Title

Recurrent impairments in visual perception and place avoidance across autism models are causally linked in the haploinsufficiency model of intellectual disability *Setd5*

Authors

Laura E. Burnett[1], Peter Koppensteiner[1], Olga Symonova[1], Tomás Masson[1], Tomas Vega-Zuniga[1], Ximena Contreras[1], Thomas Rülicke[2], Ryuichi Shigemoto[1], Gaia Novarino[1], Maximilian Jösch[1*].

Affiliations

[1] Institute of Science and Technology Austria; Am Campus 1, 3400 Klosterneuburg, Austria.

[2] Department of Biomedical Sciences and Ludwig Boltzmann Institute for Hematology and Oncology, University of Veterinary Medicine; Veterinärplatz 1, 1210 Vienna, Austria.

*Corresponding author. Email: maxjosch@ist.ac.at

Abstract

Despite the diverse genetic origins of autism spectrum disorders (ASDs), affected individuals share strikingly similar and correlated behavioural traits that include perceptual and sensory processing challenges. Notably, the severity of these sensory symptoms is often predictive of the expression of other autistic traits. However, the origin of these perceptual deficits remains largely elusive. Here, we show a recurrent impairment in visual threat perception that is similarly impaired in three independent models of ASD with different molecular aetiologies. Interestingly, this deficit is associated with reduced avoidance of threatening environments - a non-perceptual trait. Focusing on a common cause of ASDs, the *Setd5* gene mutation, we define the molecular mechanism. We show that the perceptual impairment is caused by a potassium channel (Kv1) mediated hypoexcitability in a subcortical node essential for the initiation of escape responses, the dorsal periaqueductal grey (dPAG). Targeted pharmacological Kv1 blockade rescued both perceptual and place avoidance deficits, causally linking seemingly unrelated trait deficits to the dPAG. Our findings reveal a link between rapid perception controlled by subcortical pathways and appropriate learned interactions with the environment, and define a non-developmental source of such deficits in ASD.

Introduction

Autism spectrum disorders (ASD) are conditions characterised by challenges with social interactions and repetitive behaviours, reflected in inadequate responses to others' mental states and emotions[1,2]. These alterations in social cognition co-occur with disordered sensory processing[3], a widespread yet often overlooked feature across ASD observed in every sensory modality[4]. In the visual domain, affected individuals frequently exhibit difficulties with visual attention and hyper- or hyposensitivity to visual stimuli[5], and mounting evidence suggests that the circuits involved in visual information processing are disrupted[6]. For example, atypical neuronal responses to faces and looming stimuli have been observed in individuals with ASD[7–9]. Such sensory deficits directly affect visually-guided behaviours such as gaze control, which emerges at a few months of age[10] and forms a prominent diagnostic feature[11]. Changes in gaze dynamics to subliminal stimuli[12] indicate that neuronal circuits mediating subconscious visual responses are affected, pointing towards subcortical circuits, particularly the superior colliculus (SC)[6,13,14].

Deficits in sensation are seemingly separate phenomena from the more studied cognitive impairments in ASD, believed to arise from cortical malfunctions[15–17]. However, their close association indicates the possibility of a common underlying thread, particularly because their severity is associated with the strength and expression of other ASD traits[18–20]. Such evidence has recently implicated SC pathway impairments with atypical sensory and cognitive processing[6,14]. Given this evidence, we decided to directly explore the relationship between sensation and cognition in ASD within an innate, robust and reproducible sensorimotor transformation known to be mediated by the SC - the looming escape response (LER)[21,22]. Using *Setd5[23]* as a case study, we show that the LER is impaired, not due to direct sensory or motor deficits. While all animals immediately detect the looming stimulus and can respond vigorously to a threat, they require longer to initiate the escape response than their wild-type siblings and do not form an appropriate aversion to the threat area. These two behavioural traits are highly correlated. The stronger the perceptual deficits, the weaker the avoidance. We further show that these behavioural correlations are also present in aetiologically distinct ASD mouse models (*Cul3[24]* and *Ptchd1[25]*), indicating that these various molecular dysfunctions converge on common behavioural deficits. In *Setd5,* these deficits emerge through changes in the intrinsic excitability due to an increased potassium channel conductance of neurons in the dorsal periaqueductal grey (dPAG), a structure known for commanding escape responses and receiving direct input from the SC[26,27]. Rescuing this hypoexcitability phenotype in the dPAG in adult mice recovers both the perceptual and place avoidance deficits, linking a sensorimotor disorder via a defined molecular mechanism to cognitive dysfunction. Our results show that dPAG dysfunctions can be instrumental in the emergence of symptoms associated with ASDs and that some of the dysfunctions are not developmental, opening a path for their targeted treatment.

Results

Delayed looming escape responses

To investigate whether subcortical visuomotor transformations could be affected by genetic mutations associated with ASD, we evaluated the behavioural responses to the innate looming escape response (LER) paradigm. LER is largely independent of cortical input, requiring the SC and its downstream targets to initiate appropriate responses. For this purpose, we tested a genetic haploinsufficiency ASD mouse model affecting the *SET-domain containing 5 (Setd5)[23],* a histone-associated protein found in ~1 % of patients with intellectual disability and ASD[23]. We subjected mutants (i.e., *Setd5*$^{+/-}$) and their wild-type (WT) siblings to our LER paradigm, where mice would automatically trigger a sequence of five consecutive looms upon entering a threat zone (Fig. 1a, b, see methods). For all experiments, we only used animals without any craniofacial abnormalities, tooth displacement, or eye abnormalities, which are described to sometimes occur in our *Setd5* mutant animals[23]. As previously reported, *Setd5*$^{+/-}$ animals were, on average, slightly smaller than their WT siblings[23]. Please note that other models for the same gene show more drastic abnormalities not observed in our hands[28]. During the acclimatisation period, all animals showed similar exploratory behaviour and dynamics (Fig. S1a-g), and seemingly similar behavioural responses, escaping to the shelter upon stimulus presentation (Video S1). However, behavioural differences between the genotypes became evident when observing their reaction times (Fig. 1c). While WT siblings responded robustly to the first stimulus presentation, their heterozygous siblings required, on average, more repetitions to elicit an escape response (Fig. 1d), triggered more looms (Fig. 1e), made more shelter exits (Fig. 1f), had longer reaction times and escaped with less vigour, reaching lower maximum speeds[29] (Fig. 1g). The differences across genotypes were independent of the location, speed of the animal at stimulus onset or heading angle (Fig. S1h-j), or sex (Fig. 1c-j - females, and Fig. S1l-n - males). The difference in response reaction time is an intrinsic and not an adaptive property, since it is present from the first loom presentation the animal encounters (Fig. 1hg, left). However, the escape vigour of the *Setd5*$^{+/-}$ animals during these first-ever encountered loom presentations was indistinguishable from their WT siblings (Fig. 1h, right). This indicates that the escape delay differences are not due to intrinsic motor problems, but emerge due to perceptual decision-making deficits - the process of extracting and integrating sensory information to initiate a subsequent action. These results highlight the LER as a robust behavioural assay to probe perceptual impairments and their underlying circuit dysfunctions in visuomotor processing in ASD.

To test whether the delay in initiating an escape to the loom was due to the mutant mice simply detecting the stimulus later than their WT siblings, we examined the immediate change in the speed of the animals from the time of the first loom, selecting only the trials where the mice performed an escape to the shelter at any point during the looming events. For trials where the animals generated an escape within the first loom presentation, both WT and mutant animals increased their speed significantly upon stimulus onset (Fig. 1i). For trials where the mice didn't generate an escape within the first loom, which was the majority of trials for mutant animals but only a small fraction of trials for WT animals (Fig. 1d), the mice significantly reduced their speed in the time immediately following the stimulus onset (Fig. 1J). This demonstrates that *Setd5*$^{+/-}$ animals detect and respond to the stimulus within a similar time frame as their WT siblings, but preferentially perform a locomotor arrest instead of an escape response (see Supplementary Videos). This arrest behaviour is more reminiscent of risk assessment behaviour as previously shown for loom stimuli of different contrast[29] rather than the defensive freezing response characterised by the sustained cessation of all movement, since the animals were still performing small movements of their head and upper body. Indicating that the animals are using this time to perform ongoing threat evaluation. This suggests that the

delay in LER arises from difficulties in either evaluating the threat level of the stimulus or initiating an appropriate response.

Given that cortical malfunctions have been suggested as the cause of sensory differences in autism[15–17] and that the visual cortex has been shown to modulate the response magnitude of looming sensitive cells in the SC[30], we tested whether the behavioural responses are affected in cortex and hippocampus-specific conditional *Setd5* animals (*Setd5*$^{+/fl}$; *Emx1*-Cre, Fig. S2). These animals showed no behavioural differences in their reaction times and vigour, or response kinetics (Fig. S2c-f), in line with previous studies that show that subcortical pathways[29,31], namely the SC and PAG, and not altered top-down modulation from cortical areas, are required for this behaviour.

Repetitive looming escape responses

Although the innate LER does not require learning, repeated loom presentations cause adaptive behavioural changes, for example, the emergence of place avoidance of the threat zone[29]. Given that *Setd5*$^{+/-}$ mice triggered three times more looming events and shelter exits than their WT siblings (Fig. 1e,f), we explored if altered adaptation to repeated presentations could account for the observed difference in average reaction time and vigour (Fig. 1g). For that purpose, we compared the intrinsic behavioural characteristics and the effect of the LER on the exploration strategies and behavioural adaptations across days (Fig. 2a-d). Before stimulus exposure, both cohorts had similar exploratory strategies (Fig. S1a-g), indicating that their innate exploration strategies and thus, intrinsic levels of anxiety, cannot account for the differences in reaction time and vigour. After stimulus exposure, WT animals showed expected reductions in their exploratory behaviour following the initial exposure to the looming stimulus, making fewer exits than during the pre-stimulus exploration time (Fig. 2b), eliciting fewer looms in total (Fig. 2c) with relatively constant reaction time (Fig. 2d). Strikingly, *Setd5*$^{+/-}$ consistently triggered more looms and had no signs of sensitisation upon repeated exposures (Fig. 2a-d). After the initial decrease in exploration following the first stimulus presentation, they showed no further consolidation of place avoidance to the threat zone. The reaction time and vigour of the escape response remained longer and slower across days (Fig. 2d), respectively, indicating that *Setd5*$^{+/-}$ do not sensitise as their WT siblings do to the LER paradigm. We next tested if the delayed perceptual decisions (Fig.1) are related to the consolidation of place avoidance, two seemingly independent behaviours. We analysed the total number of shelter exits for each animal and compared them with their average reaction times and vigour (Fig. 2e,f). Surprisingly, the strength of the place avoidance was a strong predictor of the reaction times, but not vigour, suggesting that the timing of the perceptual decision and the formation of place avoidance are intrinsically linked. To assess the limits of response adaptation and to ascertain if the presence of a reward would overcome the fear, we conducted the same behavioural experiment but with the presence of a food reward on the far side of the arena within the threat zone (Fig. 2g-j), and with no inter-stimulus interval restriction. Although WT siblings did make some attempts to retrieve the food reward, they quickly sensitised, rarely leaving the shelter and were unsuccessful in obtaining the food reward. *Setd5*$^{+/-}$, on the other hand, increased their shelter-leaving events, often persisting until reaching the reward (Fig. 2g-i, Video S2). Despite the rapid and repeated exposure, *Setd5*$^{+/-}$ mice continued to escape to the shelter upon stimulus presentation, for >10 consecutive presentations (Fig. 2h-j). Their reaction times showed a mild adaptation (Fig. 2j, top), while vigour remained largely constant (Fig. 2j, bottom). These results show that two behavioural traits, LER and place avoidance, strongly correlate, suggesting they share a common neuronal pathway.

Convergent behavioural deficits across ASD models.

To test whether the deficiencies observed are specific to *Setd5*$^{+/-}$ animals or might reveal a more general behavioural phenomenon across ASD models with distinct molecular and genetic aetiologies, we decided to test two additional highly penetrant mutations, *Cullin3* (*Cul3*), a ubiquitin ligase-encoding gene, and *Ptchd1* (Fig. S3a-c), a member of the Patched family speculated to function as a Sonic hedgehog receptor[25]. We exposed sex-matched sibling pairs from these models to the same LER protocol as used for the *Setd5* model and observed qualitatively similar behavioural deficits in reaction time (*Ptchd1*: Fig. 3a-d; *Cul3*: Fig. 3I-l) and place avoidance (*Ptchd1*: Fig. 3e-g; *Cul3*: Fig. 3i-l). Both cohorts required, on average, more repetitions to elicit an escape response (Fig. 3a,b & i,j), had longer reaction times between the stimulus start and the maximum speed (Fig. 3c,k), displayed slower maximum speed compared to their WT siblings (Fig. 3d,l), triggering more looms (Fig. 3e,m) and leaving the shelter more often (Fig. 3f,n), but had no differences in their behavioural strategies prior to the first loom presentation (Fig. 3g, o, Fig. S3d,k). Similar to *Setd5*, these changes were not due to the animals not reacting to the first stimulus, as seen in their consistent arrest behaviour (Fig. S3e,l), nor to differences in their exploratory behaviour (Fig. S3d,k). This difference in response reaction time is an intrinsic and not an adaptive property since it is present during the first loom presentation (Fig. S3g,n). However, they varied in strength, with *Cul3*$^{+/-}$ mice showing a less severe phenotype than the *Setd5*$^{+/-}$ or *Ptchd1*$^{Y/-}$ models. Interestingly, slower reaction times and reduced vigour could also be observed in *Ptchd*$^{Y/-}$ animals, despite their baseline hyperactivity (Fig. S3di). Interestingly, in both cohorts, the strength of the place avoidance and the reaction times were significantly lower and longer, respectively (Fig. 3c,f,k,n), being linearly correlated in *Ptchd1*$^{Y/-}$, but not *Cul3*$^{+/-}$ (Fig. 3h,p). These results suggest a general link between the timing of the perceptual decision and the formation of place avoidance, despite different molecular and developmental origins.

Deep medial SC, not retinal drive, is linked to delay in LER

Changes in average reaction times have previously been shown to depend on the saliency of the threat stimulus. Whereas repeated high-contrast looming stimuli evoke strong LER, low-contrast looms drive less vigorous escapes and longer reaction times[29], suggesting that deficits in visual processing could underlie the behavioural differences observed in *Setd5*$^{+/-}$. This possibility is aggravated by the fact that the expression of genes involved in eye development are known to be misregulated in *Setd5*$^{+/-}$ animals[23]. To explore possible visual response changes, we recorded visually evoked responses across different layers of the SC, using 32-channel silicon probes in head-fixed, awake-behaving animals (Fig. S4a), and determined the recording depth using current source density analysis (Fig. S4b-c). In our setup, mutant and control animals had similar running probabilities and showed similar baseline firing properties (Fig. S4d). We next assessed visual response properties to full-field flashes, visual stimuli that drive all neurons similarly, irrespective of their receptive field positions. First, we show that pupil dynamics are unaffected across genotypes (Fig.S 4e). Next, when clustering visually responsive cells into 10 clearly defined groups, we could observe similar proportions and identical response properties (Fig. S4f-g). Identical responses were also observed in their spatio-temporal receptive fields and the proportion of ON and OFF-responsive cells (Fig. S4a-g). Direction-selective responses (Fig. S4h,i) were also indistinguishable across groups. Finally, we explored the response properties to looming stimuli across SC layers. Looms elicit robust and reproducible firing across genotypes (Fig. 4j), with similar firing, peak rates and time-to-peak responses across genotypes (Fig. S4k-m). The overall response kinetics (Fig. S4n) and the adaptation in average firing rates across presentations (Fig. 4o,p) were indistinguishable across genotypes. The lack of any reportable visual response difference across the SC layers indicates that retino-colliculuar visual processing is largely unaltered and excludes the possibility that sensory processing can account for the observed visuomotor

deficits and suggests that the main cause of the behavioural difference may reside in downstream areas. Given that optogenetic stimulation of deep medial SC (dmSC) neurons that project to the dorsal periaqueductal grey (dPAG) generates robust escape responses and that the dPAG encodes for the choice of escape and controls the escape vigour[29], we hypothesised that activating dmSC neurons would reveal behavioural differences between genotypes and delineate the underlying circuit impairments. To test this, we focused on the *Setd5* mouse line and used unilateral *in vivo* channelrhodopsin-2 (ChR2) activation of VGluT2^{+} cells in the dmSC (Fig. 4a-c). In line with previous findings, activation of dmSC neurons in *Setd5*$^{+/+}$ animals instructed immediate shelter-directed escapes (Fig. 4d) and were absent in controls (Fig. S5). Gradually increasing the laser power and, thus, optogenetic activation, led to corresponding decreases in the latency to respond and an increase in the escape vigour in *Setd5*$^{+/+}$ (Fig. 4e). By contrast, activation of dmSC neurons in the *Setd5*$^{+/-}$ background more often resulted in an initial arrest, followed by shelter-seeking escape responses (Fig. 4f,g), mimicking the behavioural divergence observed for LER (Fig. 1). Interestingly, this behavioural difference was evident only during strong optogenetic activations. At lower laser intensities, both genotypes exhibited a transition from arrest to weak escape behaviours (Fig. 4h) with similarly low reaction time (Fig. 4e,g) and vigour (Fig. 4h). Correspondingly, the escape probabilities were identical at low optogenetic stimulation, but diverged with increased laser power (Fig. 4i). Given that changes in the strength of optogenetic activation mimic LER to looms of different contrast[29], we hypothesised that when probing animals to LER of different contrasts, both genotypes should show similar responses at lower contrast (Fig. 4j). To test this, we performed the LER at three different contrast levels: 98 %, 50 %, and 20 % (Fig. 4k,l). As predicted, the LER to low-contrast looms did not differ across genotypes, showing similar reaction times (Fig. 4k). Remarkably, in *Setd5*$^{+/-}$ animals, the reaction time remained largely constant across contrast levels (Fig. 4f,g), suggesting that the time required to initiate a response is independent of stimulus intensity. Together with the persistence of the arrest behaviour even at high levels of optogenetic activation (Fig. 4h), this supports the idea that there is a functional bottleneck downstream of the sensory processing circuits within the SC that impairs the timely generation of escape responses.

dPAG neurons are hypoexcitable in the *Setd5* mouse model

Since our previous results point towards a disruption in the circuits downstream of the SC, we decided to investigate if the activity of the underlying dPAG is affected in the *Setd5*$^{+/-}$ model (Fig. 4). To test if any synaptic or intrinsic properties of dPAG neurons are impaired, we performed whole-cell patch-clamp recordings in slices (Fig. 5a). First, using the same animals used for optogenetic stimulation *in vivo*, we tested if the synaptic properties of dmSC inputs to the dPAG are changed. 10 Hz *ex vivo* optogenetic activation elicited monosynaptic excitatory postsynaptic current (EPSC) with an average current of −244±9.65 pA in *Setd5*$^{+/+}$ and -228±11.8 pA in *Setd5*$^{+/-}$ (Fig. 5a,b). At this frequency, repeated stimulations showed no facilitation in both genotypes (Fig. 5b), indicating that dmSC inputs to the dPAG are unaltered. Next, we explored spontaneous neurotransmission by recording sEPSCs (Fig. S6a-e), supporting the view that the synaptic properties remain similar at a circuit level. Finally, we probed the intrinsic properties of dPAG neurons. These experiments were done blind to the cell type, but we were able to classify them based on their firing statistics as excitatory and inhibitory[32] (Fig. S6f-j). Although the membrane potential, input resistance, membrane constant, and capacitance were identical between genotypes (Fig. 5c), we observed a stark decrease in the ability of these cells to generate action potentials in response to injected current in both excitatory and inhibitory neurons (Fig. 5d, Fig. S6h), without affecting the rheobase (Fig. S6k). These changes were accompanied by changes in the spike shape of Setd5$^{+/-}$ animals (Fig. 5e,f) that showed slightly

265 higher depolarisation, lower after-hyperpolarisation and slower rise dynamics in comparison
266 to their WT siblings (Fig. S6i,j). Based on prior work, we know that stronger dPAG activation
267 leads to more vigorous escapes and that the underlying biophysical mechanisms depend on
268 dPAG neuronal synaptic integration and excitability[29]. Thus, intrinsic excitability changes
269 in excitatory neurons are a proxy of the expected escape strength. Remarkably, the response
270 characteristics of dPAG neurons in *Setd5*$^{+/+}$ *and Setd5*$^{+/-}$ match their behavioural differences
271 (Fig. 1). At weak current-injections (Fig. 5d), optogenetic activation (Fig. 4d-h) or low contrast
272 looms (Fig. 4k), both genotypes are indistinguishable from each other. However, at stronger
273 current-injections *Setd5*$^{+/+}$ *and Setd5*$^{+/-}$ diverge, with an hypoexcitability phenotype for
274 *Setd5*$^{+/-}$ (Fig. 5d) that matches the delay in LER for optogenetic (Fig. 4d,f) and visual (Fig. 1,
275 Fig. 4k) activations. To determine if the hypoexcitability phenotype was present in the
276 preceding visual pathway, we patched dmSC interneurons (Fig. S6l-q). Here, no statistical
277 significance was observed despite a hypoexcitability trend, indicating that the strength of the
278 effect is area-specific but not ruling out other brain-wide deficiencies. In combination with
279 previous work[29] and our optogenetic experiments (Fig. 4), these results suggest intrinsic
280 deficits in the dPAG account, at least partly, for the delayed LER phenotype in the *Setd5*$^{+/-}$
281 mice (Fig. 1).

282 ***dPAG cells are hypoexcitable due to K_v channel misregulation***

283 Next, we investigated the underlying mechanisms of the hypoexcitable phenotype of the
284 *Setd5*$^{+/-}$ dPAG cells. The changes in excitability and spike kinetics are indicative of differences
285 in channel composition that are part of adaptive homeostatic mechanisms[33], suggesting the
286 influence of voltage-gated potassium channels (Kv). Previously published work[23], which
287 studied the transcriptomic changes brought about by a mutation in *Setd5*$^{+/-}$, highlighted
288 significant upregulation in the expression of Kv1.1 channels during development. To test
289 whether the blockade of Kv1.1 would rescue the hypoexcitability phenotype, we applied
290 100 nM of **α**-Dendrotoxin (**α**-DTX), a specific Kv1.1, Kv1.2 and Kv1.6 blocker, and patched
291 dPAG cells. While **α**-DTX had no effect on *Setd5*$^{+/+}$ excitability of dPAG cells, strikingly,
292 *Setd5*$^{+/-}$ cells reversed their hypoexcitability phenotype to WT levels (Fig. 5g-h). In addition,
293 after **α**-DTX application, the spike dynamics remained identical in *Setd5*$^{+/+}$, whereas *Setd5*$^{+/-}$
294 became faster, mimicking the WT properties (Fig. 5i-j). These differences are not due to an
295 overexpression of Kv channels. Tissue-specific proteomic analysis showed no difference in the
296 protein level of Kv channels in either the PAG (Fig. 5k), SC (Fig. S7a) or cortex (Fig. S7b).
297 This is in accordance with immunohistochemical (Fig. S7c-f) and western-blot analysis (Fig.
298 S7g,h). Given that Kv1.1 has been recently shown to be involved in the homeostatic control of
299 firing[33,34] through modulation of the axon initial segment (AIS)[35], these results indicate
300 that the deficits might not arise due to direct changes in expression but due to homeostatic
301 misregulation. Next, we tested if the dPAG neurons of *Ptchd1*$^{Y/-}$ and *Cul3*$^{+/-}$ animals showed
302 similar physiological properties to *Setd5*$^{+/-}$ neurons. As expected from the molecular
303 differences among the tested ASD models, the physiological characteristics differed. *Ptchd1*
304 animals, despite having mostly identical intrinsic properties to their WT siblings (Fig. S8a-d),
305 also show a hypoexcitability phenotype at high current inputs (Fig. S8e-i,s). However, this
306 hypoexcitability phenotype cannot be rescued by **α**-DTX application (Fig. S8s). *Cul3* animals
307 did not show any changes in either their current-firing relationship or intrinsic properties (Fig.
308 S8j-r,u,v). Overall, these results indicate that different models might have distinct
309 neurodevelopmental origins or key molecular changes that give rise to particular behavioural
310 traits. In particular, for *Setd5,* Kv1 channels appear as key players and targets to reverse the
311 delayed LER phenotype and probe the causality of its correlation with place avoidance deficits.

312 To investigate whether the area-specific dPAG hypoexcitability phenotype mediated the
313 delayed LER, we tested whether **α**-DTX application targeted directly to the dPAG could rescue

the behavioural phenotype (Fig. 6a). We implanted cannulas above the dPAG in *Setd5*$^{+/-}$ and their WT littermates, a target-specific approach as visualised through neurobiotin injections (Fig. 6b). Initially, we injected saline as a control in both cohorts and subsequently tested the LER (Fig. 6c,d, top). As previously demonstrated (Fig. 1), *Setd5*$^{+/-}$ animals responded slower than their WT littermates and had no difference in their maximal escape speed during the first presentation day (Fig. 6d, top). However, the behaviour of both cohorts were indistinguishable from each other when **α**-DTX was applied, escaping immediately after the loom presentation (Fig. 6c,d, bottom, Video S3), with similar reaction times (Fig. 6e) and vigour (Fig. 6f), even despite *Setd5*$^{+/-}$ animals normally adapting across days (Fig. 2d). We then quantified the shelter exits of both cohorts (Fig. 6g,h) to investigate whether the correlation between shelter exits and delayed LER (Fig. 2e) could have a common origin. Remarkably, *Setd5*$^{+/-}$ animals recovered their place avoidance as well after **α**-DTX application (Fig. 6h), indicating that the timely initiation of actions and memory formation are closely linked. These results suggest that perceptual deficits can have far-reaching consequences for unrelated behavioural traits.

Discussion

Autism spectrum disorders (ASDs) are widespread in the global population, but our understanding of the disorder's origins remains limited. Advancements in genetic sequencing technologies have enabled the isolation of autism-risk genes, opening the door to several in-depth studies into the molecular mechanism of action of these genes[36]. However, there is a considerable mismatch between the observed wealth of molecular changes and our understanding of their roles in changing circuit function and, correspondingly, behaviour. The latter is particularly relevant since ASD is diagnosed by a combination of behavioural traits known as diagnostic criteria[2]. Although several behavioural paradigms are being studied across mouse models[37], the variability and experimental intricacies of behavioural studies make direct comparisons across models difficult. This has led to studies focusing on single models, defining particular changes but not general principles[38]. Furthermore, these studies have primarily centred on the intricacies of social interactions, communication, and repetitive behaviours—complex traits that present a formidable challenge in establishing a clear connection between neuronal dysfunction and behavioural manifestations. Here we show that the study of innate defensive behaviours, a perceptual task, provides a convergent behavioural framework that enables the directed analysis of the underlying sensorimotor processes up to the molecular level, permitting comparative dissections of the neuronal dysfunctions across ASD models and a systematic understanding of the neuronal mechanisms underlying the co-occurrence of behavioural traits. This is particularly interesting as the severity of sensory and perceptual impairments has been strongly linked to the strength and expression of traditional, non-sensory ASD traits [18–20].

Defensive escape behaviours are among the most fundamental perceptual decisions performed by animals [22]. Their finely-tuned mechanisms are indispensable for survival, but also for properly interacting with the environment. Whereas some stimuli unambiguously signal an imminent threat and should instruct immediate action, others are ambiguous and require adaptive responses arbitrated by the current context and state to decide, e.g., between ignoring, freezing, fighting, or escaping[22]. In mice, behavioural escape decisions are known to be initiated by the dPAG[29], where appropriate escape decisions are thought to be determined. While all tested ASD models can, in principle, respond behaviourally as robustly as their WT siblings, they require longer and respond with less vigour once an action has been initiated, hampering their ability to develop an appropriate place avoidance to the threat zone (Figs. 1-3). The underlying changes were rigorously dissected in the *Setd5* haploinsufficient model, pointing to a specific misregulation of voltage-gated potassium channels in dPAG neurons that gives rise to a strong hypoexcitability phenotype (Figs. 3-5), namely Kv1.1, Kv1.2 and Kv1.6.

363 Targeted pharmacological rescue of this hypoexcitability *in vivo* completely reverses the
364 behavioural phenotype (Fig. 6). This is an important finding since other brain areas are also
365 known to be required for proper defensive responses, in particular, freezing, such as the
366 pathway to the basolateral amygdala (BLA) via the lateral posterior thalamus (LP)[9,39]. Our
367 results indicate a specific involvement of the dPAG and not the BLA via LP pathway.

368 In addition to the delayed LER, we observed a strong reduction in place avoidance to the threat
369 zone that elicited maladapted repetitive behaviour (Fig. 2, Suppl. Video 2). This suggests that
370 ASD mouse models either have deficits in fear memory formation or are intrinsically less
371 fearful, thus, incapable of appropriately interpreting the noxiousness of the threatening
372 experience (Figs. 1, 2, Video S1, S2)—maladaptive behaviours that recapitulate some human
373 ASD traits[40]. Interestingly, this reduction of place avoidance is directly linked with longer
374 reaction times to the LER across ASD models (Fig. 2e, 3h, p), and thus, with the dPAG
375 hypoexcitability phenotype (Fig. 5d). We show that this correlation is causally linked, given
376 that the target-specific pharmacological rescue reverses both, the delayed LER and place
377 avoidance to wild-type levels (Fig. 6, Suppl. Video 3). Thus, maladaptive perceptual decisions,
378 as with the delayed LER, can profoundly affect seemingly independent behavioural traits, such
379 as LER, threat-induced place avoidance and the emergence of repetitive behaviours (Videos
380 S1 & S2). This is in line with studies in humans. Threat imminence has been shown to elicit
381 PAG activation[41] and the electrical stimulation of midbrain structures elicited strong
382 emotional reactions[42]. In rodents, the dPAG has been shown to support fear learning[43],
383 particularly in contextual conditioning paradigms[44]. Overall, our results emphasise the role
384 of subcortical pathways through the PAG in the altered perceptual abilities frequently described
385 in ASD, and fear memory formation in general.

386 The dPAG hypoexcitability phenotype indicates that the integration and action initiation
387 required for adequate perceptual decision-making is disrupted in *Setd5* animals. This
388 physiological phenotype is tightly linked with behavioural impairments. Substantial threat
389 evidence, either by strong optogenetic activation of dmSC neurons or high-contrast visual
390 looms, elicit a slower and less robust response in *Setd5*$^{+/-}$ compared to their WT siblings. On
391 the other hand, limited threat evidence, either by weak optogenetic activation or low-contrast
392 looms, instructs similar behavioural responses between genotypes (Fig. 4). Accordingly, only
393 strong current-injections that match the expected dPAG drive caused by high contrast loom[29]
394 cause a Kv-channel induced hypoexcitability phenotype (Fig. 5), indicating that the delayed
395 response phenotype is due to a dPAG dysfunction. This stimulus strength relationship aligns
396 with the coping difficulties of many individuals with ASD to salient sensory stimuli, such as
397 bright lights or crowded places, but not to mellow sensory environments[6]. Recently, changes
398 in dPAG excitability and the expression of defensive behaviours have also been identified in
399 the *Nlgn3*$^{+/-}$ rat model of autism [42]. Notably, these rats exhibit the inverse behavioural and
400 physiological phenotype to that observed in *Setd5*$^{+/-}$ mice, displaying stronger responses
401 auditory fear conditioning, prolonged place avoidance and hyperexcitability in dPAG cells.
402 These complementary results reflect the wide range of sensory sensitivities observed in the
403 human population with ASD, and reinforce the PAG as an important area to investigate
404 disrupted sensory processing and its far-reaching effects in the core symptomatology associated
405 with autism.

406 Given that the expression levels of Kv channels remain unaltered (Fig. 5k, Fig. S7), the causes
407 of the physiological hypoexcitability phenotype probably arise through homeostatic
408 misregulation, either by localisation[33], post-translational modifications[45], or interactions
409 with auxiliary subunits[46]. The link between potassium channels and autism is well
410 established[47]. Genetic analyses of individuals with ASD uncovered deleterious mutations in
411 potassium channels[47]. These, however, exclude Kv1.1. However, autistic-like repetitive and

social behaviours in the *Scn2a* haploinsufficiency mouse model have been rescued in a Kv1.1 deficient background[48], supporting our results that enhancing and not disrupting Kv1.1's contribution can be a fundamental factor in ASD.

Sensory processing and perceptual abnormalities have been shown to co-occur with classical ASD diagnostic criteria and have been recently proposed as promising behavioural biomarkers of autism[4]. Here we show that the innate looming escape response (LER) provides a reliable and quantitative framework to systematically link behavioural traits with the underlying molecular changes. The exact molecular alterations are dependent on the model. Whereas *Setd5* and *Ptchd1* dPAG neurons show a hypoexcitability phenotype via different mechanisms, the weaker LER deficits in *Cul3* are independent of dPAG intrinsic properties (Fig. S8). Importantly, we show that in the *Setd5* haploinsufficient model, these behavioural traits are not necessarily developmental since they can be ameliorated pharmacologically in adulthood. This is an encouraging result that may reveal therapeutic targets as envisioned by precision medicine approaches[36].

In summary, our work links innate LER dysfunctions across diverse genetic mouse models of ASDs. Specifically, in the *Setd5* haploinsufficient model, we found that a key behavioural node, the PAG[49], functions as an interface between sensory, limbic and motor circuits that, when disrupted, causally affects seemingly unrelated behaviours. This appears to be related to observations in people with ASD, where the severity of sensory processing impairments is related to the severity of core symptoms associated with autism[18–20]. Future studies designed to dissect the causal relationships between innate sensorimotor deficits, such as LER, and core ASD behavioural symptoms, such as social and communication difficulties, will be a revealing avenue to build a comprehensive view of ASD.

Materials and Methods

Mice

The study was discussed and approved by the institutional ethics committee of the University of Veterinary Medicine Vienna and the Institute of Science and Technology Austria in accordance with good scientific practice guidelines and national legislation under license numbers BMWF-68.205/0023-II/3b/2014 and 66.018/0017-WF/V/3b/2017. Male and female adult *Setd5*$^{+/-}$, *Setd5*$^{+/fl}$::*Emx1*-Cre, *Setd5*$^{+/-}$::*VGluT2*-ires-Cre, *Cul3*$^{+/-}$, *Ptchd1*$^{Y/-}$ mice were housed under a 12h light/dark cycle (lights on at 07:00), with food and water available ad libitum. The animals were housed in groups of 2-6 animals per cage and were tested during the light phase. Animals used for the *in vivo* electrophysiological recordings or freely-moving optogenetics experiments were group housed before surgery and individually housed after the surgery. Mice were chosen based on genotypes. Sex-matched animal pairs of control-mutant siblings from the same litters were compared to decrease variance due to age, environment and genetic background.

Generation of Ptchd1$^{Y/-}$ mice

Ptchd1$^{Y/-}$ mice for analysis were generated using the CRISPR/Cas9 system, as described in[50]. In brief, *in vitro* transcribed sgRNAs targeting the exon 2 of *Ptchd1* were microinjected into zygotes of C57BL/6NRj mice together with Cas9 *mRNA*. Offspring were screened by PCR for deletions using primers spanning the target sites (5′-GTAGGGCTGGAATCATGAGG-3′, 5′-CACATCCTTTGGTGTGATGC-3′). Deletion of *Ptchd1* exon 2 was confirmed by Sanger sequencing analyses. The founder line was established from a female *Ptchd1*$^{+/-}$ mouse with a 1.26 kb deletion. Analysis of *Ptchd1* transcript level by RT-PCR confirmed impaired *Ptchd1* expression in brain, cerebellum and kidney of the *Ptchd1*$^{Y/-}$ mice, compared to control mice.

Behavioural procedures

Experimental setup. All behavioural experiments were performed at mesopic light levels, in a square, black, IR-transparent Perspex box (W: 32 cm x L: 32 cm x H: 32 cm) with a shelter made of the same material (9 cm x 9 cm x 3 cm) positioned in one corner. One wall of the box was 2 cm shorter to allow for ventilation and for the optic fibre to pass through for optogenetic experiments. A plastic screen covered with a plastic sheet with a matte surface was placed as a lid on top of the box, and a modified Texas Instruments DLP projector (DLP CR4500EVM) back-projected a grey background. The blue LED was exchanged for a high-power UV-LED (ProLight 1W UV LED, peak 405 nm) to improve the differential stimulation of S pigments. The experiments were recorded with a near-IR camera (acA1920-150um, Basler, 60 Hz) from below the centre of the arena. Video recording, visual and optogenetic stimulation were controlled using custom software written in MATLAB, python and Arduino. The entire apparatus was housed within a sound-deadening, light-proof cabinet which was illuminated by an infrared light-emitting diode (LED) lamp (SIL 616.21, Sanitas).

Standard looming escape response (LER) protocol. All animals were habituated to the test arena at least one day before testing and were allowed to explore the arena for at least 20 mins. The initial 10 min of this exploration time was recorded and used to analyse the animals' exploratory behaviour (Fig. S1). For the looming avoidance response (LER: Figs.1, 2, 3, 6, S1, S2, S3) paradigm, responses were tested over five consecutive days. On each test day the animals were given 10 min to acclimatise to the arena, after which they were subjected to 3 test trials, with a 3 min interval between each trial. Each trial lasted 180 s, within which the central position of the mouse was tracked online (Python) and was used to trigger the visual stimuli in a closed-loop manner whenever the mouse crossed a designated threshold distance (10 cm)

482 from the centre of the shelter, with a minimum stimulus interval of 30 s. A typical experiment
483 lasted ~30 min and the entire arena was cleaned with 70 % ethanol between animals.

484 *LER protocol with a food reward*. In preparation for the reward trials, after the 4th day of testing
485 a small piece of banana chip was placed in the opposite corner of the arena to the shelter and
486 the mice were free to explore the arena without triggering any loom stimuli. The animals were
487 left to explore until they successfully acquired the banana chip, after which time both the mouse
488 and the chip were placed back in their home cage. The reward trial then took place after the 5th
489 day of testing. Another small piece of banana chip was again placed in the opposite corner of
490 the arena and the animals were free to explore, however this time whenever the mouse passed
491 the threshold distance from the shelter a looming stimulus would start, this time with no inter-
492 stimulus interval. For different contrast experiments, animals were presented with looming
493 stimuli of 20, 50 or 98 % contrast in a pseudorandom order upon crossing the trigger threshold.
494 The background luminosity remained constant while the luminance of the disc was increased
495 to generate low contrast stimuli.

496 *LER protocol with different contrast stimuli.* Mice were similarly habituated to the arena as in
497 the standard LER experiments; however, animals underwent a single session of three LER tests
498 over one day. In contrast to the standard LER protocol, in these experiments, upon entering the
499 threat zone they were exposed to looming stimuli of 20, 50 or 98% contrast in a pseudorandom
500 order. The background luminosity remained constant while the luminance of the disc was
501 increased to generate low contrast stimuli.

502 *In vivo optogenetic activation experiments*. The same behavioural arena was used for the
503 optogenetic activation experiments except with the standard shelter exchanged for an open
504 shelter consisting of a black piece of perspex (9 cm x 5 cm) positioned 10 cm above the floor.
505 Mice were similarly acclimatised to the arena, as in the LER procedure, but with the fibre optic
506 cable (200 µm, 0.48 NA, Doric Lenses) attached via a rotary joint (RJ1, ThorLabs) to allow for
507 unrestrained movement and minimal handling of the animals. Since it has previously been
508 shown[29] that increasing light intensity can be used as a proxy for the level of mSC, and hence
509 dPAG, activation we decided to systematically modulate the laser light intensity in different
510 trials. Once the trial began, mice were photostimulated (473 nm, 10 light pulses of 10 ms at
511 10 Hz; Shanghai Dream Lasers Technology) if they passed the threshold distance (10 cm) from
512 the shelter, with a minimum inter-stimulus interval of 30 s. The initial laser intensity was set
513 to a low irradiance (0.01-0.1 mW mm^{-2}) that did not evoke an observable behavioural response,
514 then increased to 0.5, 5, 10, 15 and 20 mW mm^{-2} with at least 3 tests (180 s each, with a
515 maximum of 5 trials per test) at each intensity. Two mice never elicited an observable escape
516 behaviour, and post-processing histological analysis revealed mislocalised or the absence of
517 viral expression in these animals and they, along with their matched siblings, were excluded
518 from the analysis.

519 *In vivo cannula experiments*. The same behavioural arena was used for the cannula experiments
520 with α-dendrotoxin (α-DTX). Two weeks after mice were implanted with the cannula, they
521 were acclimatised to the arena for 20 minutes and gently handled. 48 hours after acclimatisation
522 to the arena, the mice were attached to the infusion system (tubing (PlasticsOne C313CT),
523 infusion cannula (C315IS-5/SPC, 33GA, 5mm), guide cannula (PlasticsOne, C315GS-5/SF,
524 26GA, 5mm) and a 0.5 µL manual syringe (Model 7000.5, #86250, Hamilton) and placed into
525 an open cage to allow them to move freely during the infusion of 500nL of saline with 0.1 %
526 bovine serum albumin (BSA) at 100nl min^{-1}. The mice were left for a further 5 min before
527 detaching them from the infusion system and placing them within the arena. The first 5 minutes
528 the mice were within the arena was recorded to assess the baseline activity of these animals.
529 15 minutes after the start of infusion, a single trial of the standard LER trial was initiated. 48

530 hours after the first LER trial with saline, the mice were reattached to the infusion system and
531 α-DTX (500nL, 500nM in 0.1 % BSA) was infused at 100nl min^{-1}. The mice were again left
532 for 5 minutes before being detached and placed into the arena. Baseline activity was assessed
533 by recording the first 5 minutes within the arena, then 15 minutes after the start of the infusion
534 the standard LER trial was initiated. This time, there was a 3 min gap between LER trials and
535 3 trials were conducted, as in the standard LER test. After the last test, the mice were re-
536 attached to the infusion system and infused with 500nL of a 10% solution of neurobiotin in
537 sterile saline at 100nl min^{-1}, left for 5 minutes, then detached and placed back into their home
538 cages. The animals were sacrificed 48 hours after infusion with neurobiotin and later stained
539 with Streptavidin-594 in order to confirm the location of the cannula implantation and infusion.

540 **Viruses**

541 The viruses used in this study: for optogenetic activation, adeno-associated virus (AAV)
542 AAV9-EF1a-DIO-hChR2(E123T)T159C)-EYFP-WPRE-hGH (1×10^{13} viral genomes per ml
543 (vg ml^{-1}), Addgene 35509); for control experiments, AAV9-Syn-Flex-GCaMP6m-WPRE-
544 SV40 (1×10^{13} vg/ml, Addgene 100838).

545 **Surgical procedures**

546 Mice were anesthetised with an intraperitoneal (i.p.) injection of ketamine (95 mg kg^{-1}) and
547 xylazine (4.5 mg kg^{-1}), followed by metamizol (20 mg kg^{-1}, i.p.), buprenorphine (0.05 mg kg^{-}
548 ^{1}, i.p.) and meloxicam (2 mg kg^{-1}, subcutaneous (s.c.)). If needed, isoflurane (0.5-2 % in
549 oxygen, 0.8 l min^{-1}) was used to maintain anesthesia. Fur on the top of the head was removed
550 with an electric hair remover (Braun Precision Trimmer, PT 5010) then the mice were placed
551 in a stereotaxic frame (Model 962, Kopf Instruments) and fixed using the ear bars. Eyes were
552 protected using Oleo Vital eye cream and a topical analgesic (Xylocain 2 % gel) was applied
553 with a q-tip before cutting the skin. Craniotomies of ~ 1mm diameter were made using 0.5 mm
554 burrs (Fine Science Tools) and dental drill (Foredom, HP4-917) and viral vectors were
555 delivered using pulled pipettes (World Precision Instruments, 1.4 mm OD, 0.53 mm ID,
556 #504949) made with a micropipette puller (DMZ Zeitz-puller, Germany) and delivered using
557 an automatic nanoinjector (World Precision Instruments, Nanoliter 2010) at 20 nl min^{-1}. The
558 skin was closed after surgery using surgical glue (Vetbond, 3M, #1469SB).

559 *Optogenetics experiments.* $Setd5^{+/+}$::VGluT2-ires-Cre and $Setd5^{+/-}$::VGluT2-ires-Cre sex-
560 matched sibling mice were injected with AAV9-DIO-ChR2-eYFP (see Viruses) into the left
561 dmSC (75-100 nl, ML: -0.5, AP: -0.5 to -0.7, DV: -1.45 to -1.6, from bregma). Control mice
562 were injected with 100nl of AAV9-Flex-GCaMP6m into the left dmSC at the same coordinates.
563 One optic fibre (400 µm diameter, CFMC54L02, ThorLabs) was implanted 250 µm dorsal to
564 the injection site. Fibres were affixed using light-curing glue (Optibond Universal, Kerr Dental)
565 and dental cement (SuperBond C&B Kit, Hentschel-Dental).

566 *In vivo electrophysiological recordings*. Mice were implanted with a custom-designed head
567 plate over a ~0.5-1 mm diameter craniotomy (left hemisphere, AP: 0.4 to -0.4, ML: 0.4 to 0.8
568 from lambda) and a second craniotomy (~0.5 mm) was made anterior to bregma on the right
569 hemisphere, where a reference gold pin was implanted and lowered until it touched the brain
570 surface. Both were cemented to the skull using light-curing glue (Optibond Universal, Kerr
571 Dental) and dental cement (SuperBond C&B Kit, Hentschel-Dental), with the headplate
572 additionally fixed using Charisma Flow (Kulzer GmBH). The craniotomy was covered with
573 Kwik-Cast (World Precision Instruments) to protect the underlying tissue before recording.

574 *In vivo cannula experiments.* $Setd5^{+/+}$ and $Setd5^{+/-}$ sex-matched sibling mice were implanted
575 with a single infusion cannula (C315IS-5/SPC, 33GA, 5mm) above the dorsal PAG (ML: -
576 0.5, AP: -0.8 to -1, DV: -1.5 to -1.65, from lambda). Fibres were affixed using light-curing

glue (Optibond Universal, Kerr Dental) and dental cement (SuperBond C&B Kit, Hentschel-Dental) and the skin was closed around the implant with surgical glue (Vetbond, 3M, #1469SB).

Visual Stimuli

All stimuli were created and presented using custom-made scripts in MATLAB (MathWorks, Inc.), using the Psychophysics Toolbox extensions[51] and frames were presented at a refresh rate of 60 Hz.

Arena behavioural experiments. The standard stimulus consisted of a dark disc on a grey background presented on the lid over the centre of the arena, that reached a maximum size of 40 deg/visual angle. The disc expanded over 500 ms at a speed of 80 deg s^{-1} and then remained at this size for 250 ms before disappearing and a new expanding disc appeared immediately. A maximum of 5 expanding discs were shown upon triggering the visual stimulus. A red rectangle was presented along one side of the projected image every 5th frame, onto an out-of-view section of the arena lid. An optical filter reflected this red light back towards a photodiode (PDA36A2, ThorLabs) and this information was then used for post-hoc synchronisation of the behavioural data and the stimulus.

Head-fixed in vivo electrophysiological experiments. Sensory stimuli were made using the Psychophysics Toolbox extensions in MATLAB (MathWorks, Inc.) and presented and synchronised using custom-made LabVIEW software. At each depth, the mice were exposed to one 20 min presentation of a full field shifting spatiotemporal white-noise stimulus (see [52]) in order to assess receptive fields, and two repetitions of the remaining stimuli (5 x loom bouts, moving bars, moving gratings, full-field flash). Each presentation would start with a uniform grey screen (60 s, green and UV LED intensities were set to match the sun spectrum from a mouse opsin perspective), followed by the first presentation of the looming stimulus, then the other stimuli in a pseudorandom order separated by 30 s gaps of a grey screen. White-noise "checker" stimuli were presented at 20 Hz update for 10 min. The checker size was 6.56 deg^2 and the entire grid was shifted between 0 and 3.25 deg in both x- and y-axis after every frame. Auditory monitoring of responses to a flashing point stimulus was used in real-time to gauge the rough centre of the receptive fields of the neurons being recorded and the location of the looming stimulus was positioned to overlap with this position. The looming stimulus consisted of 10 repetitions of 5 sequential, individual looming stimuli; the same stimulus previously described and used in the behavioural experiments. These loom bouts would be presented with intervals of pseudorandom lengths between 10-30 s with a grey screen in between. To assess direction selectivity, the mice were presented with full-filed moving square gratings (1.5 cycles s^{-1} temporal frequency and 0.3 cycles deg^{-1} spatial frequency) or a wide dark bar (38 deg s^{-1} speed, 6.5 deg width) in four orientations, drifting in eight different directions (separated by 45 deg) repeated twice for each orientation. Full-field ON-OFF flashes were presented in blocks of 10 repetitions of 0.5 s OFF, 1 s ON and 0.5 s OFF stimuli.

***In vivo* electrophysiology**

Data acquisition. A 32-channel silicon probe (NeuroNexus, USA, A32-OM32) was used to record extracellular spikes from different depths of the SC in *Setd5*$^{+/+}$ (n = 3), *Setd5*$^{+/-}$ (n = 3), *Cul3*$^{+/+}$ (n = 3), *Cul3*$^{+/-}$ (n = 3), *Ptchd1*$^{Y/+}$ (n = 3) and *Ptchd1*$^{Y/-}$ (n = 3) sex-matched sibling mice. At least 24 hrs after surgery, mice were placed on a suspended spherical treadmill (20 cm diameter) and head-fixed within a toroidal screen covering 190 º of visual angle which was illuminated by a DLP-light projector (Blue LED exchanged for UV 405 nm, 60 Hz) reflecting off a spherical mirror in front of the screen (see diagram in Fig. S4a). The behaviour of the animal was recorded by a near-IR camera (Basler, acA1920-150um, 30 Hz) from the reflection

of the animal in an IR-reflective heat mirror positioned 30 cm from the face of the mouse and 35 cm from the camera. Prior to recording, the probe was coated with DiI (1 mM in ethanol, Merck, #42364) for later histological confirmation of the recording site and a wire was connected to the ground pin for both an external reference and ground. The kwik-cast seal was removed, revealing the brain surface and the confluence of the overlying superior sagittal and the left transverse sinus. Care was taken to position the probe posteriorly and medially as possible without damaging the sinuses or other blood vessels. It was then zeroed at the brain surface then slowly lowered into the overlying cortex and the SC at 1 mm s^{-1} to depths between 1.2-2.2 mm. The recording was started 15 min after reaching the desired depth to allow for stabilisation. The probe was lowered to 3-4 depths per animal with 250 µm intervals, to sample from cells across the depth of the SC. Each recording took ~30 min, with the animal in the setup for ~180 min in total. Data was recorded at 20 kHz (PCIe-6321, National instruments and Intan board RHD2000 Evaluation Board version 1.0).

In vitro electrophysiology

Mice were deeply anesthetised via intraperitoneal (i.p.) injection of ketamine (95 mg kg^{-1}) and xylazine (4.5 mg kg^{-1}), followed by transcardial perfusion with ice-cold, oxygenated (95 % O_2, 5 % CO_2) artificial cerebrospinal fluid (ACSF) containing (in mM): 118 NaCl, 2.5 KCl, 1.25 NaH_2PO_4, 1.5 $MgSO_4$, 1 $CaCl_2$, 10 Glucose, 3 Myo-inositol, 30 Sucrose, 30 $NaHCO_3$; pH = 7.4. The brain was rapidly excised and coronal sections of 300 µm thickness containing the SC and PAG were cut using a Linear-Pro7 vibratome (Dosaka, Japan). Slices were left to recover for 20 min at 35°C, followed by a slow cool down to room temperature (RT) over 40 – 60 min. After recovery, one slice was transferred to the recording chamber (RC-26GLP, Warner Instruments, Holliston, MA, USA) and superfused with ACSF containing 2 mM $CaCl_2$ and 20 µM bicuculline methiodide (Tocris) at a rate of 3 – 4 ml/min at RT. In experiments using 100 nM α-dendrotoxin (Alomone Labs, Jerusalem, Israel), 0.1 % bovine serum albumin (BSA) was added to the ACSF. Glass pipettes (B150-86-10, Sutter Instrument, Novato, CA, USA) with resistances of 3 – 4 MΩ were crafted using a P1000 horizontal pipette puller (Sutter Instrument) and filled with internal solution containing (in mM): 130 K-Gluconate, 10 KCl, 5 $MgCl_2$, 5 MgATP, 0.2 NaGTP, 0.5 EGTA, 5 HEPES; pH 7.4 adjusted with KOH. Biocytin (0.2 – 0.3 %) was added to the internal solution for post hoc morphological reconstruction. Neurons of the dPAG or the dmSC were visually identified using an infrared differential interference contrast video system in a BX51 microscope (Olympus, Tokyo, Japan). Electrical signals were acquired at 20 – 50 kHz and filtered at 4 kHz using a Multiclamp 700B amplifier (Molecular Devices, San Jose, CA, USA) connected to a Digidata 1440A digitizer (Molecular Devices) with pClamp10 software (Molecular Devices). Spontaneous excitatory postsynaptic currents (sEPSCs) were recorded at –60 mV for at least 1 min. Intrinsic membrane properties and neuronal excitability were measured in current clamp mode by applying current steps from –20 to 200 pA for 1 s in 10 pA increments. Access resistance was constantly monitored between protocols and recordings with access resistances exceeding 20 MΩ or with changes in access resistance or holding current by more than 20 % were discarded. After recordings, the pipette was carefully withdrawn and the slice was transferred to 4 % paraformaldehyde (PFA) in PBS solution.

666 **Proteomics**

667 *Samples Preparation.* Six biological replicates from cortex, superior colliculus, and
668 periaqueductal gray tissue were dissected from *Setd5*$^{+/+}$ and *Setd5*$^{+/-}$ adult mice, immediately
669 frozen in liquid nitrogen, and conserved at -70°C until further processing. Tissues were Dounce
670 homogenized 15 times in RIPA buffer (50 mM Tris-HCl pH 8, NaCl 150 mM, 0.2% sodium
671 dodecyl sulfate, 0.5% p/p sodium deoxycholate, 1 % Triton X-100, 1x protease inhibitor
672 cocktail (P8849 Roche), and 1 mM phenylmethylsulfonyl fluoride (PMSF)) and centrifuged at
673 16000g 4 °C for 20 min. Supernatants were further collected and stored at -20 °C. Total protein
674 quantity was measured with the bicinchoninic acid assay (BCA) and a total amount of 30 µg
675 of protein per sample was used for mass spectrometry measurements. All samples were cleaned
676 up by SP3 using a commercial kit (PreOmics GmbH, 50 mg of beads per sample), then
677 processed using the iST kit (PreOmics GmbH) according to the manufacturer's instructions.
678 Tryptic digestion was stopped after overnight incubation and cleaned-up samples were vacuum
679 dried. Finally, samples were vacuum dried then re-dissolved with 10 min sonication in the iST
680 kit's LC LOAD buffer.

681 *LC-MS/MS analysis.* Samples were analysed by LC-MS/MS on a nanoElute 2 nano-HPLC
682 (Bruker Daltonics) coupled with a timsTOF HT (Bruker Daltonics). Samples were first
683 concentrated over an Acclaim PepMap trap column (5.0 µm C18-coated particles, 0.5 cm *
684 300 µm ID, ThermoFisher Scientific P/N 160454), then bound onto a PepSep XTREME
685 column (1.5 µm C18-coated particles, 25 cm * 150 µm ID, Bruker P/N 1893476) heated at
686 50°C and eluted over the following 125 min gradient: solvent A, MS-grade H_2O + 0.1% formic
687 acid; solvent B, 100% acetonitrile + 0.1 % formic acid; constant 0.60 nL/min flow; B
688 percentage: 0 min, 2%; 100 min, 18 %; 125 min, 35 %, followed immediately by a 5 min
689 plateau at 95 %. MS method: M/Z range = 350-1200 Th, ion mobility range = 0.7-1.4 1/K0;
690 transfer time = 60 µs, pre-pulse storage time = 12 µs, ion polarity = positive, scan mode = dia-
691 PASEF; TIMS parameters: ramp time = 100 ms, accumulation time = 100 ms; PASEF
692 parameters: ms/ms scans = 10, total cycle time = 1.16721 s, charge range = 0-5, intensity
693 threshold for scheduling = 2,500, scheduling target intensity = 20,000, exclusion release time
694 = 0.4 min, reconsider precursor switch = on, current/previous intensity = 4, exclusion window
695 mass width = 0.015 m/z, exclusion window v·s/cm² width = 0.015 V*s/cm².

696 Raw files were searched in DiaNN version 1.8.1 in library-free mode against a Mus musculus
697 proteome obtained from UniProtKB. Match-Between-Runs was turned off. Fixed cysteine
698 modification was set to Carbamidomethylation. Variable modifications were set to Oxidation
699 (M), Acetyl (protein N-term) and Phospho (STY). Data was filtered at 1% FDR. DiaNN's
700 output was re-processed using in-house R scripts, starting from the main report table. MS1
701 intensities were re-normalized using the Levenberg-Marquardt procedure to minimise sample-
702 to-sample differences. The long format main report table was consolidated into a wide format
703 peptidoforms table, summing up quantitative values where necessary. Peptidoform intensity
704 values were re-normalized using the Levenberg-Marquardt procedure and corrected using the
705 ComBat function from the sva package to remove the replicate-related batch effect. Protein
706 groups were inferred from observed peptides, and quantified using an in-house algorithm
707 which: i) computes a mean protein-level profile across samples using individual, normalised
708 peptidoform profiles ("relative quantitation" step), ii) following the best-flyer hypothesis,
709 normalises this profile to the mean intensity level of the most intense peptidoform ("unscaled
710 absolute quantitation" step); for protein groups with at least 3 unique peptidoforms, only unique
711 ones were used. Estimated expression values were log10-converted and re-normalized using
712 the Levenberg-Marquardt procedure. P-values were adjusted using the Benjamini-Hochberg
713 (FDR) method. Average log10 expression values were tested for significance using a two-sided
714 moderated t-test per samples group. Significance thresholds were calculated using the

715 Benjamini-Hochberg procedure for False Discovery Rate values of 1%, 5%, 10 and 20%. For
716 all tests, regulated protein groups were defined as those with a significant P-value and a log2
717 ratio greater than 5% of control-to-average-control ratios.

718 **Histology**

719 For fluorescent immunostainings and histological confirmation of fibre and probe locations,
720 adult *Setd5*$^{+/+}$ and *Setd5*$^{+/-}$ mice were transcardially perfused with 4 % paraformaldehyde (PFA)
721 and their brains were dissected, post-fixed overnight in 4 % PFA, washed with 1X PBS,
722 dehydrated in a 30 % sucrose solution and sectioned with a freezing microtome (SM2010R,
723 Leica) to 100 µm (for probe/fibre/cannula confirmation) and 40 µm (for immunostainings)
724 thick slices. For histological confirmation of probe and fibre locations, the sections were rinsed
725 in PBS, stained with 4',6-diamidino-2-phenylindole (DAPI; 2 mM in PBS) and mounted on
726 Superfrost glass slides in a mounting medium containing 1,4-diazabicyclooctane (DABCO;
727 Sigma, D27802) and Mowiol 4-88 (Sigma, 81381). For Kv1.1 immunostainings, tissue was
728 rinsed and then blocked for 1 hour at room temperature in a buffer solution containing 10%
729 normal donkey serum (Abcam, ab7475), 0.1 % Triton X-100 in PBS. Primary antibodies
730 (Kv1.1, Rabbit, 1:200; Rb-Af400, Frontier Institute) were diluted in a blocking buffer and
731 incubated for 48 hours at 4 oC. The tissue was then rinsed 3 times in PBS and left overnight to
732 wash at 4 oC. Secondary antibodies (Alexa-594 Donkey anti-rabbit, 1:1000; R37119, Thermo
733 Fisher) were diluted in 1X PBS and incubated for 2 hrs at room temperature in the dark, before
734 being washed three more times in 1X PBS before being counter-stained with DAPI and
735 mounted as for histological sections described above. Sections were imaged with either a
736 confocal microscope (LSM800, Zeiss), at 63X or 20X magnification, or a wide-field
737 microscope (VS120, Olympus), at 10X magnification.

738 For visualisation of the dPAG/dmSC cells recorded *in vitro* and the neurobiotin infused into
739 the cannula implanted mice, tissue sections were washed in 1X PBS for 10 minutes then a
740 solution of Streptavidin (1:100, 1 mg/ml, Thermo Fisher Scientific, S11227) in PBS with 0.3 %
741 Triton-X was added and the samples were left at 4 ºC overnight. The tissue was then washed
742 three times with PBS, in vitro slices were mounted into a custom designed chamber for thick
743 slices and imaged with a confocal microscope (LSM800, Zeiss) at 20X (90 µm projection, 2
744 µm sections) and 40X (50 µm projection, 1 µm sections).

745 **Western blot**

746 Tissue samples from the superior colliculus, periaqueductal grey (PAG) and cortex were
747 dissected from *Setd5*$^{+/+}$ (n = 3) and *Setd5*$^{+/-}$ (n = 3) mice. PAG tissue was dissected using a 2
748 mm diameter biopsy punch (ID: 2 mm, OD: 3 mm, Fine Science Tools, 18035-02). Each
749 purification was performed independently three times and samples were stored at -80 ºC until
750 further processing. Samples were Dounce homogenized 15 times with 300 mL RIPA buffer
751 (50 mM Tris-HCl, 150 mM NaCl, 0.5 % sodium deoxycholate, 1 % Triton-X, 0.2 % SDS,
752 completeTM protease inhibitor cocktail (Roche) and and 1 mM phenylmethylsulfonyl fluoride
753 (PMSF, Sigma)) using the loose pestle and sonicated for 10 seconds. The lysed samples were
754 centrifuged for 20 min at 16000 *g* and the supernatant was stored at -80ºC. Total protein
755 concentration was determined using the BCA protein assay (Pierce). Proteins were boiled for
756 5 min in Laemmli sample buffer before being separated at 200 V for 40 min using TGX stain-
757 free precast gels (Bio-Rad). Stain-free protein gels were activated with UV light for 5 min and
758 then transferred to PVDF membranes (Bio-Rad) using a turbo transfer system (Bio-Rad).
759 Membranes were blocked for 1 hr in TBST (Tris-buffered saline with 0.1 % Tween 20)
760 supplemented with 5 % bovine serum albumin (Sigma) and then incubated overnight at 4 ºC
761 with anti-Kv1.1 primary antibody (Rb-Af400, Frontier Institute, 1:100). After primary
762 antibody incubation, membranes were washed four times with TBST for 5 min and then

incubated with anti-rabbit IRDye 800CW (LI-COR Biosciences, dilution 1:4000) for 1 hr at room temperature.

QUANTIFICATION AND STATISTICAL ANALYSIS

Analysis of behavioural data

For all behavioural experiments, the initial tracking and analysis of the escape behaviour were done blind through automatic analysis scripts and the genotypes were added later when pooling the data across animals. Automatic image processing of the behavioural video frames identified the central position and the heading direction of the mouse.

Standard looming escape response protocol. Looming escape responses (LER) were assessed by analysing a peri-stimulus time period starting from 3 s before the stimulus until 10 s after the stimulus onset. The speed of the animal was calculated as a moving mean over 83 ms time bins and responses were classified as escapes if the mouse returned to the shelter within 7 s after stimulus onset and reached a maximum speed of at least 20 cm s^{-1}. Behavioural metrics were calculated by finding the mean value across all escape trials for each animal and then averaging across mice from each genotype. The maximum escape speed was calculated as the peak value of the speed trace between the onset of the escape and entry into the shelter. The reaction time of the mouse was calculated as the time from stimulus onset till the mouse reached the maximum speed during its escape back to the shelter. This reaction time was then used to group the responses of the animals depending on which loom presentation the peak of their escape response was recorded. The number of looms triggered is the total number of loom stimuli triggered across the 5 days of testing, not including the reward trial. To analyse the immediate change in speed following stimulus onset, trials were pooled across animals from each genotype. The difference between the average speed ±50 ms around the start of the stimulus (S_{at}) and the average speed in the time 300-800 ms after the start of the stimulus (S_{im}) was calculated separately for trials where the mouse initiated an escape within the presentation of the first looming stimulus or after the presentation of the first looming stimulus. Responses were categorised based on whether the S_{im} was higher (> 1 standard deviation (SD)), lower (<1 SD) or within 1 SD from the average speed at the time of triggering the stimulus (S_{at}) across all mice from the same genotype and the distribution of trials in each category was analysed using a X^2 test of independence.

Exploratory behaviour and positional controls. Exploratory behavioural metrics during the acclimatisation period were calculated from videos of the first 10 min the mice were placed within the arena. A shelter exit was defined as an episode where the full body of the mouse moved from the inside to the outside of the shelter. The maximum distance travelled during an exit was defined as the maximal distance reached in a straight line between the centre of the mouse and the centre of the shelter. The exit duration was defined as the time between when the full body of the mouse crossed over until it re-crossed the shelter boundary. The interbout interval during exploration was the time between subsequent shelter exits. The centre position of the mouse, [Xm, Ym], was used to quantify the percentage of the 10 min recorded that the mouse was either outside of the shelter, in the centre of the area (defined as a circular area, centred on the centre of the arena where the loom was presented, [X_c, Y_c], with a 7 cm radius) or at the edge of the area (defined as outside of a circular area, centred on [X_c, Y_c] with a 14 cm radius). To understand the effect of certain parameters of the mouse's position and location within the arena on its LER response we calculated the distance of the mouse from shelter (defined as the straight line distance between [X_m, Y_m] and [X_s, Y_s]) and the heading angle of the mouse at the time of stimulus start (defined as the angle (B C) between point B, the tip of the mouse's snout, A, the position between the two back paws of the mouse and C the centre

of the shelter, [X_s,Y_s]). The position of the mouse's body parts was located using DeepLabCut tracking[53].

Looming escape response protocol in the presence of a food reward. Food reward experiments were analysed with the same scripts as the standard LER experiments. When quantifying the reaction time and maximum speed only trials where the animals met the escape criteria were included. Four *Setd5*$^{+/-}$ trials were removed from the final analysis because the mouse was interacting with the banana chip reward during the stimulus presentation. The number of looms and number of exits over the reward trials were calculated as the mean across animals from of the total per animal across genotypes.

Different contrast experiments. Trials were grouped by stimulus contrast and pooled across animals from the same genotype. A repeated measure ANOVA analysis followed by a Bonferroni correction for multiple analyses, was used to assess the effect of stimulus contrast on reaction time across genotypes and individual X^2 tests of independence were used to assess the distribution of trials into the three response categories based on the change in immediate speed for each contrast. Only trials that fulfilled the escape criteria of having returned to the shelter within 7s of stimulus onset and reaching a maximum speed of >20 cm s^{-1} were included in the analysis.

In vivo cannula experiments with α-DTX. Trials were pooled across animals from each genotype and only trials that met the escape criteria used in the standard LER trials were included in the analysis of reaction time and maximum escape speed. Shelter exits were quantified as the average number of shelter exits per animal over the LER trials either with saline or with α-DTX. Comparisons of *Setd5*$^{+/+}$ or *Setd5*$^{+/-}$ animals with saline versus α-DTX were done with paired *t*-tests if the data reached the normality criteria, otherwise paired Wilcoxon's rank sum tests were used. Unpaired Wilcoxon's rank sum tests were used for comparisons across genotypes.

Analysis of optogenetics experiments

Trials were grouped according to the laser power used and pooled across animals from each genotype. As in the analysis of the LER experiments, the speed of animal was calculated across an 83 ms time bin and the effect of laser stimulation was assessed by comparing the mean speed of the animal ±50 ms around the onset of the laser (S_{at}) and 300-800 ms after the onset of the laser (S_{im}). Trials from the 0.01 mW mm^{-2} condition were not subject to the escape criteria since laser stimulation at this intensity did not elicit an observed response, however, trials from all other laser power conditions had to meet the escape criteria used in the standard LER experiments in order to be included in further analyses. Trials were grouped by laser power intensity and S_{at} and S_{im} were compared for all trials by paired Wilcoxon signed-rank tests. Similar to the LER analysis, responses were individually grouped based on both the sign and the magnitude of the difference between S_{at} and S_{im}, into three groups where S_{im} is either more than 1 standard deviation (SD) greater than S_{at}, more than 1 SD less than S_{at} or within 1 SD of S_{at}. Chi-Square tests were used to compare the distribution of the *Setd5*$^{+/+}$ and *Setd5*$^{+/-}$ trials at different laser powers.

For the control experiments, with GcaMP injected mice (Fig. S5) the Log_{10}(**Δ**Speed) was calculated as the logarithmic of the ratio between S_{im} and S_{at}. The change in Log_{10}(**Δ**Speed) across laser powers was analysed using a two-way repeated measures ANOVA looking at the effect of genotype, laser power and their interaction, followed by a multiple comparisons analysis with Bonferroni correction.

855 **Analysis of *in vivo* silicon probe recordings**

856 *Preprocessing.* Initial analysis was performed in MATLAB R2018b and later in MATLAB
857 R2019a. Raw voltage traces were high-pass filtered (300 Hz) and spikes were detected and
858 sorted using Kilosort2 (https://github.com/cortex-lab/Kilosort) and Phy as previously
859 described[54], followed by manual curation. Firing rates histograms were calculated as the
860 average firing rate across 16.7 ms time bins. Analog input channels (Photodiode, camera
861 trigger) were extracted in MATLAB (MathWorks, Inc.) and arduino were recorded at a 20 kHz
862 sample rate and were used for offline synchronisation. Custom-made scripts in MATLAB were
863 used to extract the time points of the visual stimulus onsets and matched them to the
864 corresponding video camera frame.

865 *Determining the surface of the superficial superior colliculus (sSC).* Initial SC location was
866 determined in real-time by auditory monitoring of multi-unit activity to a flashing stimulus and
867 was later confirmed offline using a current source density analysis of the raw recording
868 (see [31,55]) combined with histological reconstruction of the probe location visualised with
869 DiI. CSD profiles were calculated for each recording and were used to align the depth of the
870 units across recordings and across animals. The transition point between an overlying source
871 and underlying sink was taken as the boundary between the stratum griseum superficiale (SGS)
872 and the stratum opticum (SO). The boundary between the superficial (sSC) and
873 intermediate/deep superior colliculus (idSC) was defined as 100 µm below this inflection depth
874 (ID), taking into account the thickness of the SO. sSC was defined as 300 µm above the ID to
875 100 µm below the ID, and idSC was defined as the area below 100 µm below the ID. Only
876 units identified as within the sSC and units with at least 2 spikes within the stimulus
877 presentation were used for analysis. For all analyses spikes were sorted into peristimulus
878 periods based on synchronisation with the stimulus frames and firing-rate histograms were
879 calculated over 16.7 ms time bins.

880 *Analysis of baseline firing properties.* Responses to a full field grey screen during the first 60s
881 of recording were taken to determine the baseline firing properties of the recorded cells. The
882 baseline firing rate per animal was calculated as the mean firing rate across cells in the 1000 µm
883 below the sSC surface.

884 *Analysis of responses to flash stimulus.* Responses to a single flash stimulus (0.5 s OFF; 1 s
885 ON; 0.5 s OFF) were generated by averaging the firing-rate histograms across 10 repetitions
886 of the stimulus. The responsiveness of single units was defined based on the p-value generated
887 from running a ZETA test[56] on the average firing rate histograms using the 30 s period before
888 the stimulus as baseline and the 2 s flash stimulus as the response time. Clustering of responsive
889 units was done using K-means and the number of clusters was determined by identifying the
890 elbow point when analysing the Calinski-Harabasz index. Clustering was done with units from
891 both genotypes pooled together, then later split based on genotype. The proportion of flash-
892 responsive cells for *Ptchd1* and *Cul3* animals were determined for each animal by dividing the
893 number of sSC units that were $p < 0.05$ by the total number of sSC units found.

894 *Analysis of responses to loom stimulus.* Responses to a single loom stimulus were obtained by
895 averaging the responses to the first loom of the loom bout stimulus (consisting of 5 consecutive
896 looms) across 10 repetitions. Responsiveness was again defined as units having a *p*-value
897 (determined using the ZETA test) of < 0.05, with the 30 s preceding the loom stimulus as
898 baseline and the 0.7 s of first loom presentation as the response time. The average firing rate
899 was calculated as the overall average of the mean firing rate recorded across each of the 5 loom
900 presentations individually for 10 repetitions. Maximum firing was similarly calculated as the
901 mean maximum firing during each of the 5 looms, averaged across 10 repetitions. The time-to-

902 peak was calculated as the mean of the time to the peak firing within each of the 5 looms,
903 averaged over the 10 repetitions.

904 *Analysis of responses to shifting white noise stimulus.* To further analyse the visual receptive
905 fields (RFs) of the units recorded we analysed their responses to a shifting white noise
906 stimulus[52] and calculated them as spike-triggered averages. The location of the centre of the
907 receptive field was estimated by finding the pixel with the highest variance over a peri-spike
908 time period and the final RF was cropped to 160 x 160 pixels centred on this pixel with highest
909 variance. Signal-to-noise ratio (SNR) for each neuron is defined as
910 $10 \cdot log_{10}(max_{power}/noise_{power})$, where max_{power} is the square of the pixel value at the receptive
911 field centre, and $noise_{power}$ the variance of all the values in a 5 pixels border around the edge of
912 the RF. Visually-responsive neurons were defined as those with SNRs in the 80th percentile of
913 the SNRs of all sSC units or above. The centre of the RF was assigned as ON or OFF based on
914 the sign of the mean of the central pixel at the centre of the receptive field. The proportion of
915 OFF RFs was calculated as the ratio between visually-responsive cells with OFF RFs and the
916 total number of visually-responsive cells in the sSC. The radius of the RF centre was calculated
917 as the width at half-peak of the spatial RF profile. The average radius of the receptive fields of
918 an animal was calculated using only the visually-responsive units. Temporal receptive fields
919 were clustered similarly to flash responses, using K-means to cluster the responses and the
920 number of clusters was determined using the Calinski-Harabasz index.

921 *Analysis of responses to moving bars and gratings stimuli.* For each direction the mean across
922 trials was calculated and normalised to the baseline firing in the 30 s before stimulus onset. The
923 preferred direction (D_p) was defined as the direction with the greatest normalised response and
924 the non-preferred direction (D_{np}) was taken as 180 degrees from that angle. The direction
925 selectivity index (DSI) was then computed as $(D_p-D_{np})/(D_p+D_{np})$ with values falling in a range
926 from 1 (high direction selectivity) to 0 (low direction selectivity). Units were defined as being
927 'direction selective' (DS) if their DSI was in the 80th percentile or higher out of all units
928 recorded within the sSC. The proportion of direction selective cells per animal was found by
929 quantifying the proportion of DS sSC units divided by all sSC units recorded for that animal.

930 *Analysis of behavioural data from head-fixed visual stimulation.* The motion of the animal was
931 determined by sorting the difference between pixels in neighbouring frames with K-means into
932 two groups. The proportion of time each animal spent running was calculated as the proportion
933 of frames that were registered as 'moving' over the total number of frames. The pupillary light
934 reflex (PLR) of the animals was assessed by tracking the change in pupil size across the
935 repetitions of the flash stimulus. A deep neural network approach for markerless tracking[53]
936 was used to extract points around the pupil. The diameter of the pupil was then calculated by
937 fitting an ellipse to these points. Since we observed, and it is known, that the size of the pupil
938 is greatly affected by locomotion, when analysing the PLR we only included repetitions in
939 which the mice were running. An animal was considered to be running during a repetition if
940 the mouse was classified as 'moving' in over half of the video frames covering that repetition.

941 **Analysis of in vitro patch clamp electrophysiological recordings**

942 Whole-cell recordings were analysed in Clampfit (Molecular Devices) and MiniAnalysis
943 Program (Synaptosoft). Resting membrane potential (RMP) was measured as the average
944 membrane potential prior to current-injection. Input resistance (R_{in}) was calculated from the
945 slope of the linear fit of the hyperpolarising current/voltage relationship. Membrane time
946 constant τ was measured from the exponential fit of the membrane potential change in response
947 to a –10 or –20 pA current-injection. Membrane capacitance (C_m) was calculated from $C_m =$
948 τ/R_{in}. Action potential firing was quantified in Clampfit using the event detection function.
949 Phase-plane plots were performed to investigate the dynamic changes in the membrane

potential over time (dV/dt) and were generated using the spikes from the first current step necessary to elicit action potentials (rheobase current). Soma size was calculated by fitting an oval to the projected image (63X) of the neurons and calculating the area of that oval.

Analysis of proteomics

MS files were searched in DiaNN version 1.8.1 in library-free mode against a *Mus musculus* proteome obtained from UniProtKB. Match-Between-Runs was turned off. Fixed cysteine modification was set to Carbamidomethylation. Variable modifications were set to Oxidation (M), Acetyl (protein N-term) and Phospho (STY). Data was filtered at 1% FDR. DiaNN's output was re-processed using in-house R scripts, starting from the main report table. MS1 intensities were re-normalized using the Levenberg-Marquardt procedure to minimize sample-to-sample differences. The long format main report table was consolidated into a wide format peptidoforms table, summing up quantitative values where necessary. Peptidoform intensity values were re-normalized using the Levenberg-Marquardt procedure and corrected using the ComBat function from the sva package to remove the replicate-related batch effect. Protein groups were inferred from observed peptides, and quantified using an in-house algorithm which: *i)* computes a mean protein-level profile across samples using individual, normalized peptidoform profiles ("relative quantitation" step), *ii)* following the best-flyer hypothesis, normalizes this profile to the mean intensity level of the most intense peptidoform ("unscaled absolute quantitation" step); for protein groups with at least 3 unique peptidoforms, only unique ones were used, otherwise razor peptidoforms were also included; Phosphopeptidoforms and their unmodified counterparts were excluded from the calculations. Estimated expression values were log10-converted and re-normalised using the Levenberg-Marquardt procedure. P-values were adjusted using the Benjamini-Hochberg (FDR) method. Average log10 expression values were tested for significance using a two-sided moderated t-test per samples group and a global F-test (limma). Significance thresholds were calculated using the Benjamini-Hochberg procedure for False Discovery Rate values of 1 %, 5 %, 10 and 20 %. For all tests, regulated protein groups were defined as those with a significant P-value and a log2 ratio greater than 5 % of control-to-average-control ratios. GO terms enrichment analysis was performed comparing for each test regulated against observed protein groups (topGO). Statistical analysis was performed for Phospho-modified peptides as for protein groups, normalizing ratios to parent protein group(s).

Analysis of histological data

For comparison between the Kv1.1 expression in *Setd5*$^{+/+}$ and *Setd5*$^{+/-}$ tissue 30 µm stacks were imaged with 1 µm sections at 63X magnification, or 55 µm stacks were imaged with 2 µm sections at 20X magnification, and the same laser power settings were used for all images at a given magnification.

Analysis of western blot data

The Bio-Rad ChemiDoc MP system was used for imaging and acquisition and images were quantified using ImageJ software. Protein levels are displayed as fold change. Student's *t* test was used to test for significance (MATLAB, MathWorks, Inc.). Data represent mean ± SEM obtained from three mice per genotype.

Statistics

Analyses were performed in custom-written MATLAB (2019a) scripts (MathWorks, Inc.). Shapiro-Wilk and Levene's tests were used to test the normality and the equal variances of the datasets, respectively and parametric or non-parametric tests were used accordingly. Two-tailed tests were used unless specified. All statistical tests are reported in the text and appropriate Fig. legends ($^{*}p < 0.05$, $^{**}p < 0.01$, $^{***}p < 0.001$). In bar plots, the mean ± s.e.m. are shown, unless otherwise stated. Boxplots display the median and IQR.

References

1. Baron-Cohen S, Leslie AM, Frith U. Does the autistic child have a “theory of mind” ? Cognition. 1985;21: 37–46.

2. American Psychiatric Association. Diagnostic and Statistical Manual of Mental Disorders, Fifth Edition, Text Revision (DSM-5-TR(tm)). American Psychiatric Association Publishing; 2022.

3. Tomchek SD, Dunn W. Sensory processing in children with and without autism: a comparative study using the short sensory profile. Am J Occup Ther. 2007;61: 190–200.

4. Robertson CE, Baron-Cohen S. Sensory perception in autism. Nat Rev Neurosci. 2017;18: 671–684.

5. Simmons DR, Robertson AE, McKay LS, Toal E, McAleer P, Pollick FE. Vision in autism spectrum disorders. Vision Res. 2009;49: 2705–2739.

6. McFadyen J, Dolan RJ, Garrido MI. The influence of subcortical shortcuts on disordered sensory and cognitive processing. Nat Rev Neurosci. 2020;21: 264–276.

7. Kleinhans NM, Richards T, Johnson LC, Weaver KE, Greenson J, Dawson G, et al. fMRI evidence of neural abnormalities in the subcortical face processing system in ASD. Neuroimage. 2011;54: 697–704.

8. Hadjikhani N, Åsberg Johnels J, Zürcher NR, Lassalle A, Guillon Q, Hippolyte L, et al. Look me in the eyes: constraining gaze in the eye-region provokes abnormally high subcortical activation in autism. Sci Rep. 2017;7: 3163.

9. Hu Y, Chen Z, Huang L, Xi Y, Li B, Wang H, et al. A translational study on looming-evoked defensive response and the underlying subcortical pathway in autism. Sci Rep. 2017;7: 14755.

10. Jones W, Klin A. Attention to eyes is present but in decline in 2–6-month-old infants later diagnosed with autism. Nature. 2013. pp. 427–431. doi:10.1038/nature12715

11. Volkmar FR, Lord C, Bailey A, Schultz RT, Klin A. Autism and pervasive developmental disorders. J Child Psychol Psychiatry. 2004;45: 135–170.

12. Madipakkam AR, Rothkirch M, Dziobek I, Sterzer P. Unconscious avoidance of eye contact in autism spectrum disorder. Sci Rep. 2017;7: 13378.

13. Tokuoka K, Kasai M, Kobayashi K, Isa T. Anatomical and electrophysiological analysis of cholinergic inputs from the parabigeminal nucleus to the superficial superior colliculus. J Neurophysiol. 2020;124: 1968–1985.

14. Jure R. Autism Pathogenesis: The Superior Colliculus. Front Neurosci. 2018;12: 1029.

15. Pelphrey KA, Shultz S, Hudac CM, Vander Wyk BC. Research review: Constraining heterogeneity: the social brain and its development in autism spectrum disorder. J Child Psychol Psychiatry. 2011;52: 631–644.

1035 16. Buckner RL, Andrews-Hanna JR, Schacter DL. The brain's default network: anatomy,
1036 function, and relevance to disease. Ann N Y Acad Sci. 2008;1124: 1–38.

1037 17. Minshew NJ, Williams DL. The new neurobiology of autism: cortex, connectivity, and
1038 neuronal organization. Arch Neurol. 2007;64: 945–950.

1039 18. Estes A, Zwaigenbaum L, Gu H, St John T, Paterson S, Elison JT, et al. Behavioral,
1040 cognitive, and adaptive development in infants with autism spectrum disorder in the first
1041 2 years of life. J Neurodev Disord. 2015;7: 24.

1042 19. Stevenson RA, Ruppel J, Sun SZ, Segers M, Zapparoli BL, Bebko JM, et al. Visual
1043 working memory and sensory processing in autistic children. Sci Rep. 2021;11: 3648.

1044 20. Fabbri-Destro M, Maugeri F, Ianni C, Corsini S, Di Stefano E, Scatigna S, et al. Early
1045 Sensory Profile in Autism Spectrum Disorders Predicts Emotional and Behavioral
1046 Issues. J Pers Med. 2022;12. doi:10.3390/jpm12101593

1047 21. Yilmaz M, Meister M. Rapid innate defensive responses of mice to looming visual
1048 stimuli. Curr Biol. 2013;23: 2011–2015.

1049 22. Branco T, Redgrave P. The Neural Basis of Escape Behavior in Vertebrates. Annu Rev
1050 Neurosci. 2020;43: 417–439.

1051 23. Deliu E, Arecco N, Morandell J, Dotter CP, Contreras X, Girardot C, et al.
1052 Haploinsufficiency of the intellectual disability gene SETD5 disturbs developmental
1053 gene expression and cognition. Nat Neurosci. 2018;21: 1717–1727.

1054 24. Morandell J, Schwarz LA, Basilico B, Tasciyan S, Dimchev G, Nicolas A, et al. Cul3
1055 regulates cytoskeleton protein homeostasis and cell migration during a critical window
1056 of brain development. Nat Commun. 2021;12: 1–22.

1057 25. Wells MF, Wimmer RD, Schmitt LI, Feng G, Halassa MM. Thalamic reticular
1058 impairment underlies attention deficit in Ptchd1Y/− mice. Nature. 2016;532: 58–63.

1059 26. Bandler R, Depaulis A, Vergnes M. Identification of midbrain neurones mediating
1060 defensive behaviour in the rat by microinjections of excitatory amino acids. Behav Brain
1061 Res. 1985;15: 107–119.

1062 27. Deng H, Xiao X, Wang Z. Periaqueductal Gray Neuronal Activities Underlie Different
1063 Aspects of Defensive Behaviors. J Neurosci. 2016;36: 7580–7588.

1064 28. Sessa A, Fagnocchi L, Mastrototaro G, Massimino L, Zaghi M, Indrigo M, et al. SETD5
1065 Regulates Chromatin Methylation State and Preserves Global Transcriptional Fidelity
1066 during Brain Development and Neuronal Wiring. Neuron. 2019;104: 271–289.e13.

1067 29. Evans DA, Stempel AV, Vale R, Ruehle S, Lefler Y, Branco T. A synaptic threshold
1068 mechanism for computing escape decisions. Nature. 2018;558: 590–594.

1069 30. Zhao X, Liu M, Cang J. Visual cortex modulates the magnitude but not the selectivity of
1070 looming-evoked responses in the superior colliculus of awake mice. Neuron. 2014;84:
1071 202–213.

1072 31. Lee KH, Tran A, Turan Z, Meister M. The sifting of visual information in the superior
1073 colliculus. Elife. 2020;9. doi:10.7554/eLife.50678

1074 32. Pavón Arocas O. Biophysical properties and gene expression profile of single
1075 periaqueductal gray neurons. Doctoral, UCL (University College London). 2022.
1076 Available: https://discovery.ucl.ac.uk/id/eprint/10157063/

1077 33. Zbili M, Rama S, Benitez M-J, Fronzaroli-Molinieres L, Bialowas A, Boumedine-
1078 Guignon N, et al. Homeostatic regulation of axonal Kv1.1 channels accounts for both
1079 synaptic and intrinsic modifications in the hippocampal CA3 circuit. Proc Natl Acad Sci
1080 U S A. 2021;118. doi:10.1073/pnas.2110601118

1081 34. Morgan PJ, Bourboulou R, Filippi C, Koenig-Gambini J, Epsztein J. Kv1.1 contributes
1082 to a rapid homeostatic plasticity of intrinsic excitability in CA1 pyramidal neurons in
1083 vivo. Elife. 2019;8. doi:10.7554/eLife.49915

1084 35. Grubb MS, Burrone J. Activity-dependent relocation of the axon initial segment fine-
1085 tunes neuronal excitability. Nature. 2010;465: 1070–1074.

1086 36. Kostic A, Buxbaum JD. The promise of precision medicine in autism. Neuron.
1087 2021;109: 2212–2215.

1088 37. Silverman JL, Yang M, Lord C, Crawley JN. Behavioural phenotyping assays for mouse
1089 models of autism. Nat Rev Neurosci. 2010;11: 490–502.

1090 38. Willsey HR, Willsey AJ, Wang B, State MW. Genomics, convergent neuroscience and
1091 progress in understanding autism spectrum disorder. Nat Rev Neurosci. 2022;23: 323–
1092 341.

1093 39. Wei P, Liu N, Zhang Z, Liu X, Tang Y, He X, et al. Processing of visually evoked
1094 innate fear by a non-canonical thalamic pathway. Nat Commun. 2015;6: 6756.

1095 40. Macari S, DiNicola L, Kane-Grade F, Prince E, Vernetti A, Powell K, et al. Emotional
1096 Expressivity in Toddlers With Autism Spectrum Disorder. J Am Acad Child Adolesc
1097 Psychiatry. 2018;57: 828–836.e2.

1098 41. Mobbs D, Petrovic P, Marchant JL, Hassabis D, Weiskopf N, Seymour B, et al. When
1099 fear is near: threat imminence elicits prefrontal-periaqueductal gray shifts in humans.
1100 Science. 2007;317: 1079–1083.

1101 42. Nashold BS Jr, Wilson WP, Slaughter DG. Sensations evoked by stimulation in the
1102 midbrain of man. J Neurosurg. 1969;30: 14–24.

1103 43. Di Scala G, Mana MJ, Jacobs WJ, Phillips AG. Evidence of Pavlovian conditioned fear
1104 following electrical stimulation of the periaqueductal grey in the rat. Physiol Behav.
1105 1987;40: 55–63.

1106 44. Pavesi E, Canteras NS, Carobrez AP. Acquisition of Pavlovian fear conditioning using
1107 β-adrenoceptor activation of the dorsal premammillary nucleus as an unconditioned
1108 stimulus to mimic live predator-threat exposure. Neuropsychopharmacology. 2011;36:
1109 926–939.

45. Winklhofer M, Matthias K, Seifert G, Stocker M, Sewing S, Herget T, et al. Analysis of phosphorylation-dependent modulation of Kv1.1 potassium channels. Neuropharmacology. 2003;44: 829–842.

46. Niespodziany I, Mullier B, André VM, Ghisdal P, Jnoff E, Moreno-Delgado D, et al. Discovery of a small molecule modulator of the Kv1.1/Kvβ1 channel complex that reduces neuronal excitability and in vitro epileptiform activity. CNS Neurosci Ther. 2019;25: 442–451.

47. Guglielmi L, Servettini I, Caramia M, Catacuzzeno L, Franciolini F, D'Adamo MC, et al. Update on the implication of potassium channels in autism: K+ channelautism spectrum disorder. Front Cell Neurosci. 2015;9. doi:10.3389/fncel.2015.00034

48. Indumathy J, Pruitt A, Gautier NM, Crane K, Glasscock E. Kv1.1 deficiency alters repetitive and social behaviors in mice and rescues autistic-like behaviors due to Scn2a haploinsufficiency. Brain Behav. 2021;11: e02041.

49. Behbehani MM. Functional characteristics of the midbrain periaqueductal gray. Prog Neurobiol. 1995;46: 575–605.

50. Yang H, Wang H, Jaenisch R. Generating genetically modified mice using CRISPR/Cas-mediated genome engineering. Nat Protoc. 2014;9: 1956–1968.

51. Brainard DH. The Psychophysics Toolbox. Spat Vis. 1997;10: 433–436.

52. Gupta D, Młynarski W, Symonova O, Svatoň J, Joesch M. Panoramic visual statistics shape retina-wide organization of receptive fields. bioRxiv. 2022. p. 2022.01.11.475815. doi:10.1101/2022.01.11.475815

53. Mathis A, Mamidanna P, Cury KM, Abe T, Murthy VN, Mathis MW, et al. DeepLabCut: markerless pose estimation of user-defined body parts with deep learning. Nat Neurosci. 2018;21: 1281–1289.

54. Pachitariu, Steinmetz, Kadir. Fast and accurate spike sorting of high-channel count probes with KiloSort. Adv Neural Inf Process Syst. Available: https://proceedings.neurips.cc/paper/2016/hash/1145a30ff80745b56fb0cecf65305017-Abstract.html

55. Stitt I, Galindo-Leon E, Pieper F, Engler G, Engel AK. Laminar profile of visual response properties in ferret superior colliculus. J Neurophysiol. 2013;110: 1333–1345.

56. Montijn JS, Seignette K, Howlett MH, Leonie Cazemier J, Kamermans M, Levelt CN, et al. ZETA: a parameter-free statistical test for neuronal responsiveness. bioRxiv. 2021. p. 2020.09.24.311118. doi:10.1101/2020.09.24.311118

Acknowledgments

We thank Prof. Peter Jonas for his suggestion on the involvement of potassium channels and members of the Neuroethology group for their comments on the manuscript. Katalin Szigeti and Julie Murmann for experimental help. This research was supported by the Scientific Service Units of IST Austria through resources provided by the Lab Support Facility, the

Imaging and Optics Facility, the Machine Shop Unit and the Preclinical Facility, especially Freyja Langer and Michael Schunn.

Author contributions

LB and MJ designed the study. LB analysed all data with help from OS. LB performed the behavioural, optogenetic, α-DTX cannula, and *in vivo* electrophysiology experiments. PK performed the *in vitro* experiments. LB, MJ and OS developed the behavioural system and analysis pipeline. TVZ, OS and MJ developed the *in vivo* electrophysiology setup and LB the analysis pipeline. TM performed the protein level analysis. XC, GN and TR generated the *Ptchd1* mouse line. GN and RS provided mouse lines, reagents and gave advice on the study design. LB and MJ wrote the manuscript with help of the other authors.

Funding

This work was supported by a European Research Council Starting Grant 756502 (MJ).

Competing interests

Authors declare that they have no competing interests.

Data and materials availability

Proteomics, behavioural data, *in vivo* electrophysiological silicon probe data and *in vitro* electrophysiological patch clamp data will be deposited and made available as of the date of publication. Microscopy data reported in this paper will be shared by the lead contact upon request.

Figures

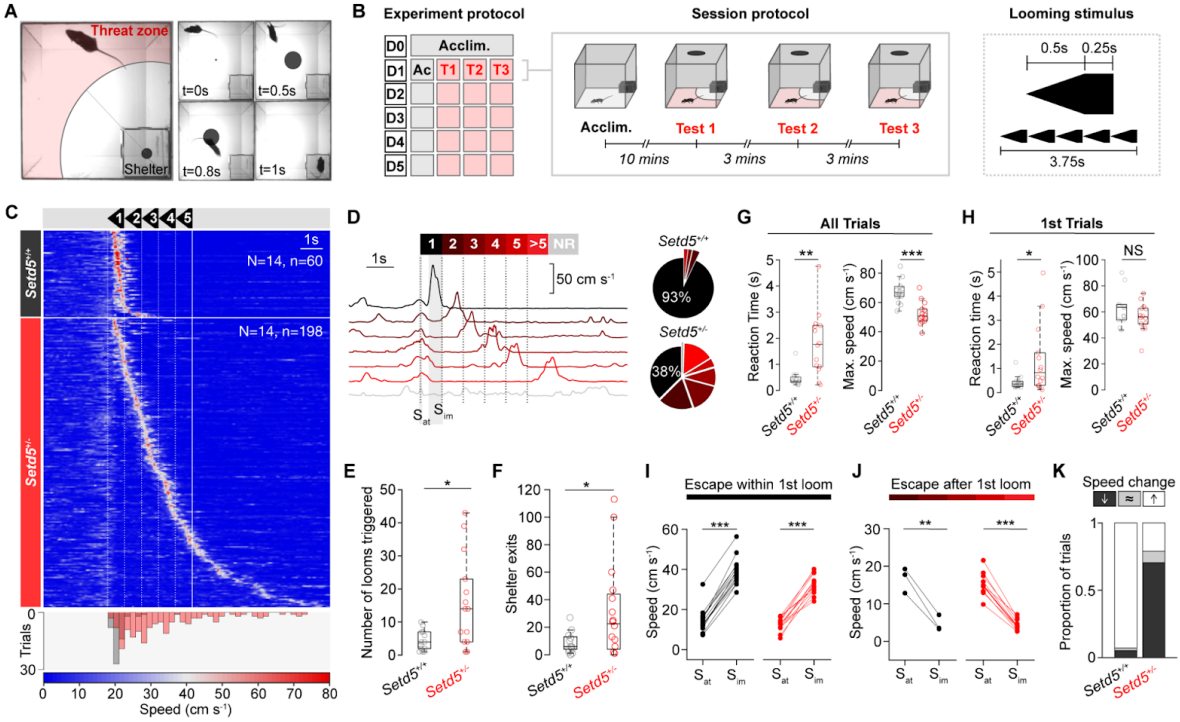

Figure 1. ASD mice exhibit delayed and less vigorous looming escape responses. a, Looming escape response (LER) paradigm showing the shelter's location and the threat zone (left) and LER example (right). **b,** Paradigm schematic. Day 0 (D0) was used for acclimatisation. D1-D5 consisted of an acclimatisation period (grey) followed by three LER tests (red). The looming stimulus consisted of 5 consecutive looms (right). **c**, Raster plot of mouse speed during LER (white, dotted vertical lines denote the start of each loom; solid white line denotes the end of the stimulus) for *Setd5*$^{+/+}$ (upper, n =14, 60 trials) and *Setd5*$^{+/-}$ (lower, n = 14, 198 trials), sorted by reaction time. Bottom, distribution of reaction times for all *Setd5*$^{+/+}$ (black) and *Setd5*$^{+/-}$ (red) trials ($p < 0.001$, two-sample Kolmogorov-Smirnov test). **d**, Left, example trials based on whether the mouse responds within 1 of the 5-loom stimuli, after the 5th (>5), or not at all (NR - no response) from one *Setd5*$^{+/-}$ mouse. Grey shaded areas represent the frames used to calculate the speed at stimulus onset (S_{at}) and the immediate response speed (S_{im}). Right, proportion of escapes to loom presentations. **e**, Total looms triggered across the 5 test days (*Setd5*$^{+/+}$, 4.36 looms; *Setd5*$^{+/-}$, 16 looms, P = 0.013). **f**, Total shelter exits across the 5 test days (*Setd5*$^{+/+}$, 6.0; *Setd5*$^{+/-}$, 24.5, P = 0.019). **g**, Average reaction time (left) and maximum escape speed (right) per animal (reaction time, P = 0.001; max. escape speed, $P < 0.001$). **h**, as (**g**), but only for the very first loom presentation (reaction time, P = 0.046; max. escape speed, P = 0.166). **i**, Average immediate speed change following the stimulus presentation for all trials where the mice escape within the first loom presentation (left, *Setd5*$^{+/+}$, n = 14, black, $p < 0.001$; right, *Setd5*$^{+/-}$, n = 14, red, $p < 0.001$). S_{at} is the mean speed of the animal ±50 ms of stimulus onset and S_{im} is the mean speed of the animal 300-800ms after stimulus onset. **j**, as (**i**) but for trials where the mice escape during or after the second loom (left, *Setd5*$^{+/+}$, n = 3, black, p = 0.007; right, *Setd5*$^{+/-}$, n = 11, red, $p < 0.001$). **k**, Proportion of response types per genotype ($X^2 = 103.9$, $p < 0.001$, X^2 test of independence). P-values: Wilcoxon's test, p-values: paired *t*-test, unless specified.

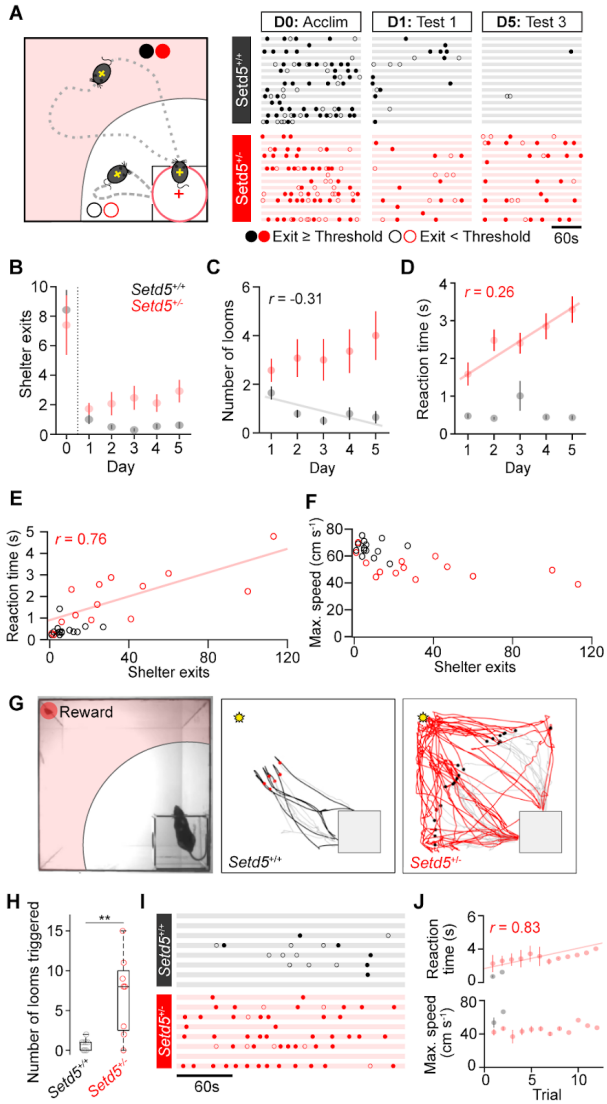

Figure 2. Altered adaptation and repetitive behavioural phenotype to the LER. a, left, Graphic depicting exits where the mouse enters (dotted line, filled dot) or does not enter (dashed line, open dot) the threat zone. Right, ethogram of exploratory shelter exit behaviour during the pre-stimulus acclimatisation, the first and last test of the LER paradigm. Each row represents one animal. **b-d,** Adaptation in the number of shelter exits, average number of looms triggered and reaction times across days (**b**, Setd5$^{+/+}$: p = 0.2189, *Setd5*$^{+/-}$: p = 0.4974; **c**, *Setd5*$^{+/+}$, p = 0.0087; Setd5$^{+/-}$, p = 0.2192; **d**, *Setd5*$^{+/+}$, p = 0.890; Setd5$^{+/-}$, p < 0.001). **e**, Relationship between the number of shelter exits and the average reaction time per animal (*Setd5*$^{+/+}$, p = 0.626; *Setd5*$^{+/-}$, p = 0.002). **f**, as (**e**) but for maximum escape speed per animal (*Setd5*$^{+/+}$, p = 0.547; *Setd5*$^{+/-}$, p = 0.053). **g**, Left, reward trial example showing the location of the food reward within the threat zone. Right, example trajectories during the reward trials show the mouse's position for the 3 s before triggering the loom (light grey) and the 6 s following the stimulus start (black or red). Filled dots represent the position of the mouse when the stimulus was triggered, grey square represents the shelter, and the yellow star shows the position of the food reward. **h**, Number of looms triggered during the reward trial (*Setd5*$^{+/+}$, 1 bout; *Setd5*$^{+/-}$, 8 bouts, P = 0.005). **i**, Ethograms of exits, as in (**a**), during the reward trials show an increased probability of *Setd5*$^{+/-}$ mice leaving the shelter during a trial (number of exits, 2.12 for *Setd5*$^{+/+}$, 6.88 for *Setd5*$^{+/-}$, p = 0.057). **j**, Reaction time (top panel, *Setd5*$^{+/-}$, 44 trials, $r = 0.828$, $p = 0.0001$) and escape vigour (bottom panel, *Setd5*$^{+/-}$, 44 trials, $r = 0.184$, $p = 0.5116$) during repeated presentations of the loom. Trials when the animal was interacting with the reward were excluded. P-values: Wilcoxon's test, p-values: Pearson's correlation test, unless specified. Plotted linear fits depict the statistically significant correlations.

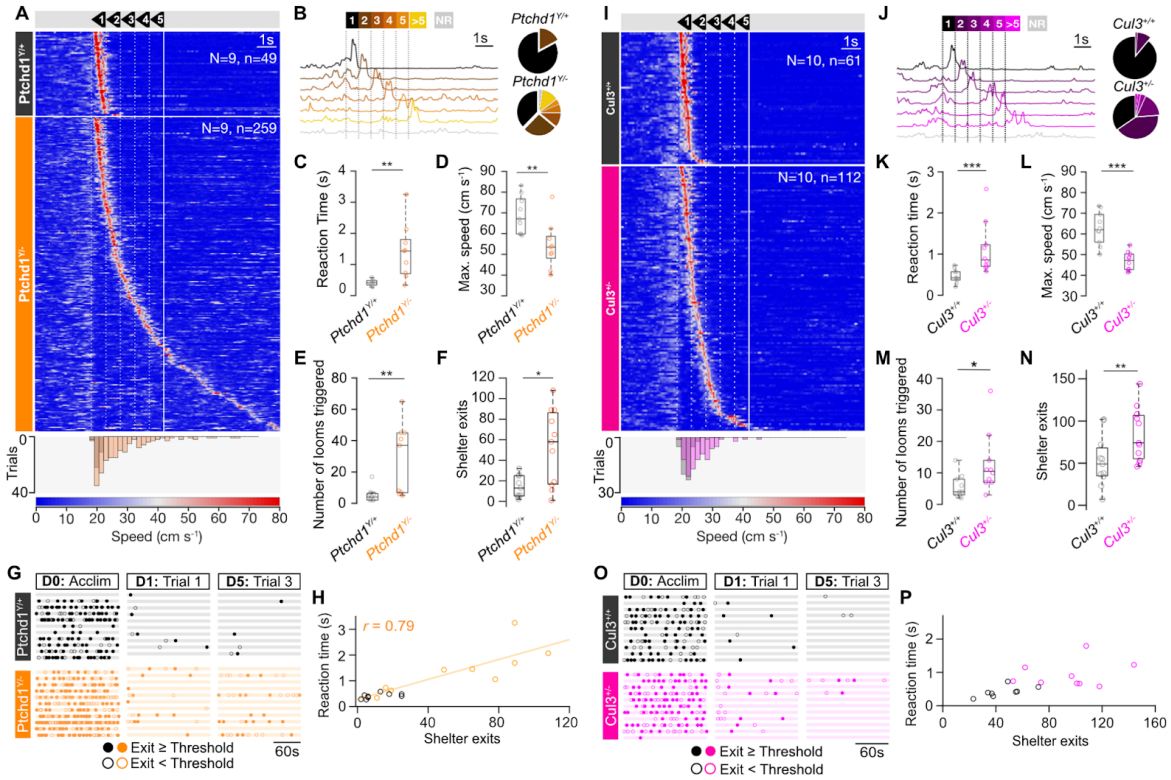

Fig. 3. Conserved behavioural changes across etiologically distinct autism models. a, Raster plot of mouse speed in response to the looming stimuli for *Ptchd1*$^{Y/+}$ (upper, n = 9, 49 trials) and *Ptchd1*$^{Y/-}$ (lower, n = 9, 259 trials), sorted by reaction time. Bottom, distribution of reaction times for all *Ptchd1*$^{Y/+}$ (black) and *Ptchd1*$^{Y/-}$ (orange) trials. **b**, Left, Left, example trials based on whether the mouse responds within 1 of the 5-loom stimuli, after the 5th (>5), or not at all (NR - no response) from one *Ptchd1*$^{Y/-}$ mouse. Right, proportion of escape to loom presentations. Trials where mice escaped within the first loom: *Ptchd1*$^{Y/+}$, 0.826, *Ptchd1*$^{Y/-}$, 0.374, p = 0.004. **c**, Average reaction time and (**d**) maximum escape speed per animal, for all trials where the mice escaped (Reaction time; *Ptchd1*$^{Y/+}$, 0.411s, *Ptchd1*$^{Y/-}$, 1.41 s, p = 0.002. Maximum escape speed; *Ptchd1*$^{Y/+}$, 69.1 cms^{-1}, *Ptchd1*$^{Y/-}$, 54.2 cms^{-1}, p = 0.005). **e**, Average total looms triggered per genotype across 5 days of testing (*Ptchd1*$^{Y/+}$, 5.44 looms; *Ptchd1*$^{Y/-}$, 28.8 looms, P = 0.004). **f**, Average total shelter exits across the 5 test days (*Ptchd1*$^{Y/+}$, 15; *Ptchd1*$^{Y/-}$, 53, P = 0.025). **g**, Ethogram of shelter exits during the pre-stimulus acclimatisation, first and last trial of the LER paradigm. Each row represents one animal, filled and open dots represent exits that crossed into the threat zone or not, respectively. **h**, Relationship between the number of shelter exits and the average reaction time per animal (*Ptchd1*$^{Y/+}$, p = 0.126; *Ptchd1*$^{Y/-}$, r = 0.76, p = 0.012, Pearson's correlation). **i-p**, same as **a-h** but for *Cul3*. **i**, *Cul3*$^{+/+}$ (top, n = 10, 61 trials) and *Cul3*$^{+/-}$ (bottom, n = 10, 112 trials. Bottom, distribution of reaction times (p < 0.001, two-way KS test). **j**, *Cul3*$^{+/+}$, 0.892, *Cul3*$^{+/-}$, 0.347, p < 0.001, two-way KS test). **k**, Reaction time; *Cul3*$^{+/+}$, 0.464 s, *Cul3*$^{+/-}$, 1.11 s, P < 0.001. **i,** Maximum escape speed; *Cul3*$^{+/+}$, 62.7 cm s^{-1}, *Cul3*$^{+/-}$, 46.8 cm s^{-1}, P < 0.001). **m**, (*Cul3*$^{+/+}$, 5.60 looms; *Cul3*$^{+/-}$, 12.9 looms, P = 0.023). **n**, (*Cul3*$^{+/+}$, 47; *Cul3*$^{+/-}$, 89, P = 0.006). **p**, (*Cul3*$^{+/+}$, p = 0.078; *Cul3*$^{+/-}$, p = 0.571, Pearson's correlation). Box-and-whisker plots show median, IQR and range. Shaded areas represent SEM. Lines are shaded areas, mean ± s.e.m., respectively. P-values are Wilcoxon's test**,** p-values: two-sample Kolmogorov-Smirnov test, unless specified.

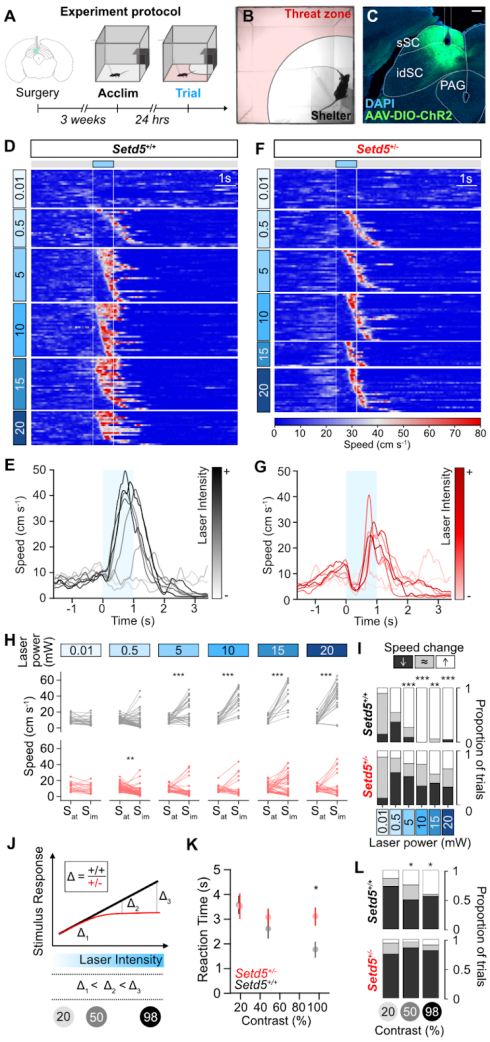

Figure 4. Activation of deep SC neurons recapitulates delayed LER in *Setd5*$^{+/-}$ animals. **a**, Timeline of the experimental protocol for optogenetic activation of the dmSC. **b**, Video frame during an optogenetics trial. **c**, Confocal micrograph of AAV-ChR2 expression in dmSC and optic fibre location reconstruction, scale bar: 200 µm. **d**, Raster plot of mouse speed in response to optogenetic activation, sorted by laser intensity and (**e**) mean speed responses at increasing laser intensities for *Setd5*$^{+/+}$ (n = 4, 312 trials). **f-g**, as (**d-e**) but for *Setd5*$^{+/-}$ mice (n = 4, 291 trials). Blue-shaded areas represent the laser stimulation. **h**. Subplots of trials in (**d, f**) showing the immediate change in speed upon light activation at different laser intensities for *Setd5*$^{+/+}$ (n = 4, paired *t*-tests) and *Setd5*$^{+/-}$ (n = 4, paired Wilcoxon's tests) optogenetics trials. S_{at} is the mean speed of the animal ±50 ms of laser onset and S_{im} is the mean speed of the animal 300-800ms after laser onset. **i**, Proportion of trials at different laser intensities that either show an increase (white), decrease (black) or no change (grey) in speed upon light activation for *Setd5*$^{+/+}$ (top) and *Setd5*$^{+/-}$ (bottom). 0.01mW mm^{-2}: 35 trials, p = 0.649; 0.5mW mm^{-2}: 111 trials, p = 0.193; 5mW mm^{-2}: 50 trials, p < 0.001; 10mW mm^{-2}: 49 trials, p < 0.001; 15mW mm^{-2}: 61 trials, p = 0.004; 20mW mm^{-2}: 49 trials, p < 0.001, X^2 test of independence. **j**, Schematic of the behavioural divergence between genotypes with increasing stimulus intensity (laser or loom). **k**, Summary of mean ± s.e.m. of reaction time to the LER paradigm at different stimulus contrasts (p = 0.021 for the interaction between genotype and contrast, *Setd5*$^{+/+}$, n = 13, 68 trials; *Setd5*$^{+/-}$, n = 13, 59 trials, repeated measures ANOVA. p = 0.018 for 98% contrast, with multiple comparisons and Bonferroni correction. *Setd5*$^{+/+}$, 24 trials; *Setd5*$^{+/-}$, 22 trials). **l**, Proportion of trials at different contrast looms that show an increase (white), decrease (black), or no change (grey) in speed upon light activation (20%: p = 0.698; 50%, p = 0.026; 98%, p = 0.021, X^2 test of independence).

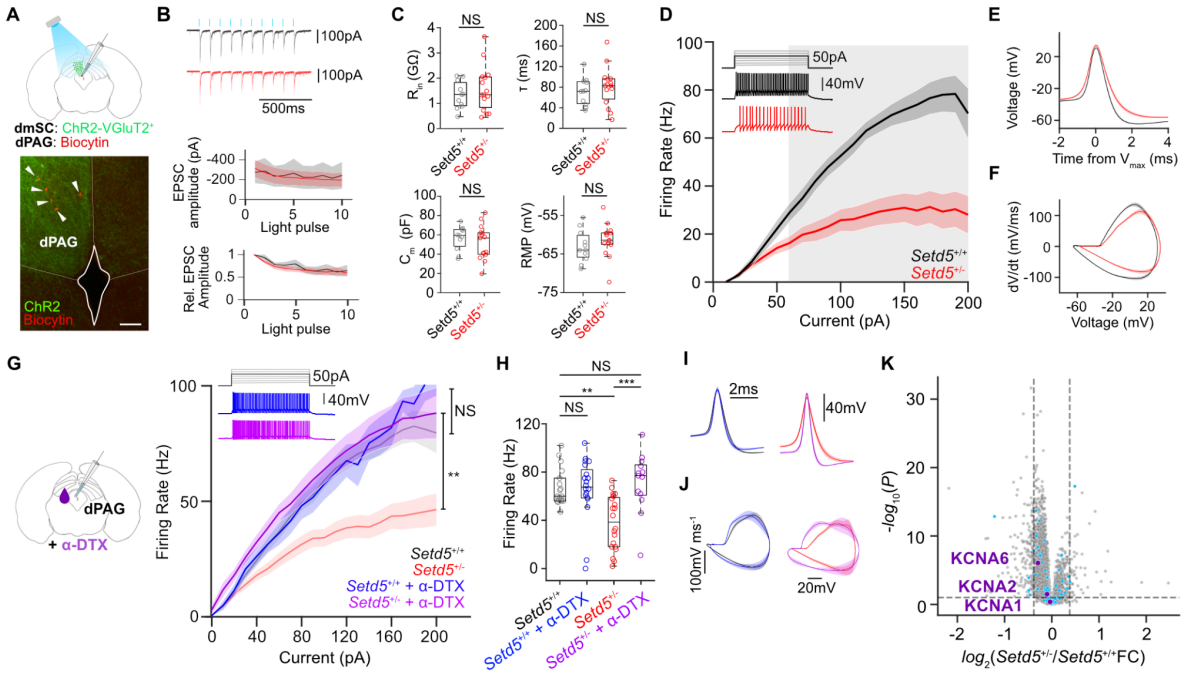

Fig. 5. *Setd5*$^{+/-}$ dPAG cells are hypoexcitable. a, Schematic of the experimental approach, *in vitro* patch clamp recordings (top) and micrograph of VGluT2^{+} dmSC projections to the dPAG infected with AAV9-ires-DIO-ChR2 (green) with dPAG biocytin filled and recorded cells (red & arrow heads, scale bar: 100 **µ**m). **b**, Top, whole-cell voltage clamp traces of example *Setd5*$^{+/+}$ and *Setd5*$^{+/-}$ cells (black and red, respectively) responding to 10 Hz light stimulation (blue ticks). Amplitude (middle, p = 0.078) and relative EPSC amplitude (bottom, p = 0.565) of responses to sequential light pulses in a 10 Hz train. **c**, Intrinsic properties of *Setd5*$^{+/+}$ (n = 6, 11 cells) and *Setd5*$^{+/-}$ (n = 7, 14 cells) dPAG cells. Input resistance (P = 0.756, top left), membrane constant tau (P = 0.436, top right), membrane capacitance (P > 0.995, bottom left) and resting membrane potential (P = 0.213, bottom right). **d**, Summary of the relationship between current injection and action potential firing for putative glutamatergic cells showing a strong reduction in firing (p < 0.001). Inset, representative example traces to a 50 pA current injection. Grey area indicates the current injection values that significantly differ between *Setd5*$^{+/+}$ cells (black) and *Setd5*$^{+/-}$ cells (red) found by a multiple comparisons analysis with Tukey correction. **e**, Average shape and (**f**) phase plane analysis of the action potentials generated in the rheobase sweep (*Setd5*$^{+/+}$, 13 cells, 42 spikes; *Setd5*$^{+/-}$, 14 cells, 72 spikes). **g**, Summary of the relationship between current injection and action potential firing for all *Setd5*$^{+/+}$ cells (black, n = 18) and *Setd5*$^{+/-}$ cells (red, n = 20) before and after (*Setd5*$^{+/+}$: blue, n =12 cells; *Setd5*$^{+/-}$: purple, n = 13 cells) application of **α**-Dendrotoxin (**α**-DTX, 100 nM, p > 0.995 and p = 0.0147 for the effect of **α**-DTX on *Setd5*$^{+/+}$ and *Setd5*$^{+/-}$ firing, respectively). Inset, representative example traces from *Setd5*$^{+/+}$ cells (blue) and *Setd5*$^{+/-}$ (purple) cells after **α**-DTX application to a 50 pA current injection. **h**, Effect of **α**-DTX on firing in response to 120pA current injection. Before **α**-DTX (*Setd5*$^{+/+}$ versus *Setd5*$^{+/-}$; p = 0.0017), effect of **α**-DTX on *Setd5*$^{+/+}$ (before versus after **α**-DTX; P > 0.995) and *Setd5*$^{+/-}$ (before versus after **α**-DTX; P < 0.001, *Setd5*$^{+/+}$ before versus *Setd5*$^{+/-}$ after **α**-DTX; P > 0.995). Multiple comparison analysis after rm-ANOVA with Tukey correction. **i**, Action potential shape and **j**, phase plane analysis of the action potentials generated in the rheobase current in *Setd5*$^{+/+}$ cells (without **α**-DTX, black, n =19; with **α**-DTX, blue, n =12), *Setd5*$^{+/-}$ cells (without **α**-DTX, red, n=21; with **α**DTX, purple, n = 13). **k**, Volcano plot for differential protein levels between adult S*etd5*$^{+/+}$ and *Setd5*$^{+/-}$ mice (n = 6 samples per genotype, cyan dots represent proteins annotated as ion-channels and purple dots represent Kv1.1, Kv1.2 and Kv1.6. Lines and shaded areas, mean ± s.e.m., respectively. Box-and-whisker plots show the median, IQR, and range. P-values are Wilcoxon's rank sum test. p-values are two-way repeated measures ANOVA. Volcano plot horizontal dashed line represents the significance threshold (P-value < 0.1) from a two-sided moderated t-test while the vertical dashed lines indicate fold change values greater or lower than 0.4 between *Setd5*$^{+/+}$ and *Setd5*$^{+/-}$.

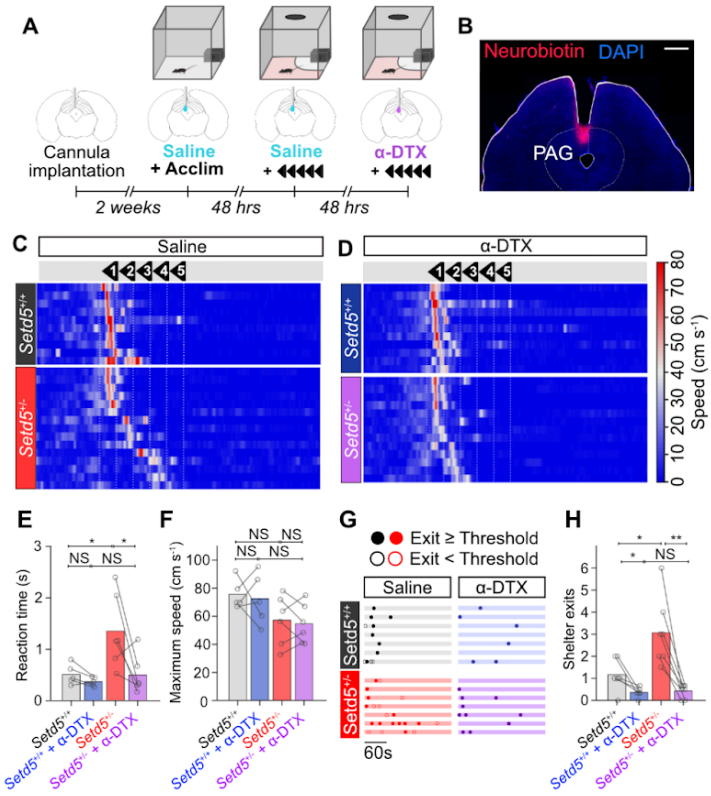

Fig. 6. Pharmacological Kv channel block rescues delayed LER and place avoidance. a, Timeline of *in vivo* **α**-DTX cannula experiments. **b**, Confocal micrograph of a coronal section of the location of the cannula above the dPAG as well as the expression of neurobiotin that was infused into the cannula at the end of the experiments. Scale bar: 500 **µ**m. **c**, Raster plots of mouse speed in response to the looming stimuli for *Setd5*$^{+/+}$ before (top, n = 6, 10 trials) and after (bottom, n = 6, 11 trials) infusion of **α**-DTX (500nL, 500nM) sorted by reaction time. **d**, as for (**c**) but for *Setd5*$^{+/-}$ before (top, n = 6, 15 trials) and after (bottom, n = 6, 13 trials) animals after infusion of **α**-DTX (500nL, 500nM). **e**, Effect of **α**-DTX on reaction time. Before **α**-DTX (*Setd5*$^{+/+}$ versus *Setd5*$^{+/-}$; P = 0.017), effect of **α**-DTX on *Setd5*$^{+/+}$ (saline versus **α**-DTX; p = 0.104) and *Setd5*$^{+/-}$ (saline versus **α**-DTX; p = 0.014) and after **α**-DTX (*Setd5*$^{+/+}$ versus *Setd5*$^{+/-}$; P = 0.571). **f**, Effect of **α**-DTX on escape vigour. Before **α**-DTX (*Setd5*$^{+/+}$ versus *Setd5*$^{+/-}$; P = 0.052), effect of **α**-DTX on *Setd5*$^{+/+}$ (saline versus **α**-DTX; p = 0.760) and *Setd5*$^{+/-}$ (saline versus **α**-DTX; p = 0.649) and after **α**-DTX (*Setd5*$^{+/+}$ versus *Setd5*$^{+/-}$; P = 0.075). **g**, Shelter exit behaviour during the first LER trial when the mice are injected with saline (*Setd5*$^{+/+}$, black, top left; *Setd5*$^{+/-}$, red, bottom left) or **α**-DTX (*Setd5*$^{+/+}$, blue, top right; *Setd5*$^{+/-}$, purple, bottom right). Each row represents one animal, filled and open dots represent exits crossed into the threat zone or not, respectively. **h**, Effect of **α**-DTX on shelter exits. Before **α**-DTX (*Setd5*$^{+/+}$ versus *Setd5*$^{+/-}$; P = 0.012), effect of **α**-DTX on *Setd5*$^{+/+}$ (saline versus **α**-DTX; p = 0.038) and *Setd5*$^{+/-}$ (saline versus **α**-DTX; p = 0.003) and after **α**-DTX (*Setd5*$^{+/+}$ versus *Setd5*$^{+/}$; P = 0.495). Markers represent the average values across all trials for individual animals. P-values: Wilcoxon's test, p-values: paired-t-test.